

Dynamics of the Galactic Bulge using Planetary Nebulæ

Sylvie F. Beaulieu¹, Kenneth C. Freeman, Agris J. Kalnajs, Prasenjit Saha²,
Mount Stromlo and Siding Spring Observatories, The Australian National University,
Canberra ACT 2611, Australia; beaulieu@ast.cam.ac.uk; kcf@mso.anu.edu.au;
agris@mso.anu.edu.au; saha@maths.qmw.ac.uk

and HongSheng Zhao

Sterrewacht Leiden, Niels Bohrweg 2, 2333 CA, Leiden, Netherlands;
hsz@strw.LeidenUniv.nl

Received _____; accepted _____

¹present address: Institute of Astronomy, University of Cambridge, Madingley Road,
Cambridge CB3 0HA, United Kingdom

²present address: Astronomy Unit, School of Mathematical Sciences, Queen Mary and
Westfield College, Mile End Road, London E1 4NS, United Kingdom

ABSTRACT

Evidence for a bar at the center of the Milky Way triggered a renewed enthusiasm for dynamical modelling of the Galactic bar-bulge. Our goal is to compare the kinematics of a sample of tracers, planetary nebulae, widely distributed over the bulge with the corresponding kinematics for a range of models of the inner Galaxy. Three of these models are N-body barred systems arising from the instabilities of a stellar disk (Sellwood, Fux and Kalnajs), and one is a Schwarzschild system constructed to represent the 3D distribution of the COBE/DIRBE near-IR light and then evolved as an N-body system for a few dynamical times (Zhao). For the comparison of our data with the models, we use a new technique developed by Saha (1998). The procedure finds the parameters of each model, i.e. the solar galactocentric distance R_{\odot} in model units, the orientation angle ϕ , the velocity scale (in km s^{-1} per model unit), and the solar tangential velocity which best fit the data.

Subject headings: Galaxy: bulge — Galaxy: kinematics and dynamics — ISM: planetary nebulae

1. Introduction

A spiral galaxy consists of a relatively flattened stellar disk in nearly circular rotation and, in most systems, a central bulge. It is estimated that about 30 % of these galaxies also show a central bar in the visible; however the real fraction of barred galaxies is probably significantly higher because some apparently normal spirals show a bar feature in the near-IR that was not visible in their optical images (e.g. Sellwood & Wilkinson, 1993). In addition, barred galaxies often show a lens and/or ring around the bar. The flattened disks contain objects of all ages, from the interstellar gas and very young stars to the old disk stars which in our Galaxy are almost as old as the globular clusters. The bulges appear to be made up mainly of old stars.

The disks of most disk galaxies are relatively thin, with the ratio of their radial to vertical scale heights mostly in the range 5 to 15. In the later-type barred galaxies, the central bar may be no thicker than the host disk. Kormendy (1993) has argued that many of the features identified as bulges from the surface photometry of more face-on galaxies may also be as thin as the disks. However, many edge-on galaxies show bulges which clearly do extend beyond the disk.

The bulges of spiral galaxies show a wide range of shapes, from spheroidal through boxy or peanut shaped bulges. The boxy versus spheroidal structure of bulges is roughly understood in terms of their orbital properties but not in terms of origin. Many possibilities have been suggested for the origin of boxiness in bulges, including the formation and dissolution of bars, dissipative processes during the collapse of a rapidly rotating inner region, or later accretion events (see Sellwood 1993; Rowley 1986; Whitmore & Bell 1988; Combes et al. 1990; Pfenniger et al. 1991).

Kormendy and Illingworth (1982) pointed out that the boxy bulges are frequently cylindrical rotators, unlike the more spheroidal bulges. This led to a burst of observational

and theoretical studies of these systems (e.g. Binney & Petrou 1985; Rowley 1986; Shaw 1993), with the growing indication that these boxy or peanut-shaped edge-on systems may be associated with bars (Combes et al. 1990; Sellwood & Wilkinson 1993).

The Milky Way has an excellent example of a box-shaped bulge. This feature was seen in the early $2.4\mu\text{m}$ balloon scans (Matsumoto et al. 1982), and spectacularly confirmed by the $2.2\mu\text{m}$ image of the Galaxy from COBE³/DIRBE^{4,5} (Weiland et al. 1994; Arendt et al. 1994) as seen from the contours plot of the COBE/DIRBE $2.2\mu\text{m}$ image (Figure 1). See Binney et al. (1997) for a dust-corrected non-parametric recovery of the light distribution in the inner few kpc of the Milky Way from the COBE/DIRBE surface brightness map.

The bulge of the Milky Way provides a unique opportunity to investigate the detailed pattern of rotation and velocity dispersion in a boxy Galactic bulge. We can study the structure of the bulge to see if this boxy bulge is really a stellar bar, and we can also see how the bulge and disk are related dynamically.

This paper is outlined as follows. We start with an overview of recent studies of the bar/bulge problem through axisymmetric and N-body models (Section 2). In Section 3, we discuss the wide range of tracers available to study the kinematics of the Galactic bulge, and the data obtained for this study. A preliminary visual assessment of the data is presented in Section 4 using the mean velocity and velocity dispersion versus the Galactic longitude and latitude. Section 5 compares our planetary nebulae (PNe) distribution with the distribution of light in the COBE/DIRBE images in the 1.25 , 2.2 and $3.5\mu\text{m}$ wavelength

³Cosmic Background Explorer

⁴Diffuse Infrared Background Experiment

⁵The COBE datasets were developed by NASA Goddard Space Flight Center under the guidance of the COBE Science Working Group and were provided by the NSSDC.

regions. In Section 6, we compare our PNe data with four Galactic bar-bulge models: three are N-body models and one is a relaxed Schwarzschild realization of the COBE light distribution. A summary and conclusions are given in Section 7.

2. Dynamics of the Bulge

2.1. The Bar/Bulge of the Milky Way

Evidence is accumulating that the boxy peanut-shaped bulges seen in edge-on disk galaxies are associated with bar structures (Combes et al. 1990; Jenkins & Binney 1994; Blitz & Spergel 1991; Kuijken & Merrifield 1995; Bureau & Freeman 1999). For the bulge of our Galaxy, the $2.4\mu\text{m}$ balloon scans and the near-IR COBE/DIRBE images show such a boxy peanut shape. An unambiguous direct identification of a bar at the center of the Galaxy is difficult because the Sun is located in the plane of the Galaxy and our view of the Galactic center is obscured by the dust. The patchy extinction in the plane of the Galaxy is obvious from the optical image of the Galactic bulge taken at ESO (Madsen & Laustsen, 1986). It is clear that the southern part of the bulge is much less affected by extinction than the northern part. The southern part includes two famous regions of relatively low extinction, Sgr I ($l = 1.4^\circ$, $b = -2.6^\circ$) and Baade's Window (BW) ($l = 1.0^\circ$, $b = -3.9^\circ$) which are widely used for studies of the stellar population and dynamics of the inner bulge. The distribution of extinction over the bulge is also nicely shown from the work of the COBE/DIRBE group (Arendt et al. 1994, figure 3b, plate L7).

Nevertheless, much observational evidence is now pointing to the existence of such a bar. Here, we list only a few: see Gerhard (1999) for a more detailed review.

- de Vaucouleurs (1964) was the first to point out that a central bar is probably responsible for the non-circular motions of the HI in the inner part of the Milky Way.

He had already noted that similar non-circular motions were present in the inner parts of barred spiral galaxies.

- The asymmetry in longitude of the distribution of the $2.4\mu\text{m}$ emission derived from the balloon scans indicated that the stars in the central kpc lie in a bar with its near side at positive Galactic longitude and suggested that the bar is tilted relative to the Galactic plane (Blitz & Spergel 1991).
- The COBE/DIRBE images (Weiland et al. 1994) confirmed the asymmetry in the surface brightness distribution of the bulge in the near-IR, but show no evidence for an out-of-plane tilt of the bar.
- Nikolaev & Weinberg (1997) reported that the distribution of variables in the IRAS Point Source Catalogue (PSC) is consistent with a bar with semi-major axis of 3.3 kpc and position angle of $24^\circ \pm 2^\circ$ (where position angle is the angle between the major axis of the bar and the Sun-center line and is taken as positive for a bar pointing into the positive Galactic longitude quadrant).
- Rohlfs and Kampmann (1993) showed that the HI terminal velocities indicate the presence of a bar with a semi-major axis of 2 – 3 kpc and a position angle of about 45° .
- Binney et al. (1991) used CO kinematics in the inner parts of the Galaxy to show the presence of a bar with a pattern speed of $63 \text{ kms}^{-1}\text{kpc}^{-1}$, a corotation radius of 2.4 kpc and a position angle of $16^\circ \pm 2^\circ$. More recent gas dynamical studies (Englmaier & Gerhard 1999; Weiner & Sellwood 1999; Fux 1999) all support for a substantially larger corotation radius.

From some of these studies, and others on the brightnesses of tracer objects like Mira variables (e.g. Whitelock 1993) and clump giants in the bulge (e.g. Stanek et al. 1994), it seems fairly clear that the bulge objects at positive Galactic longitude are brighter than

those at negative longitude. This is generally interpreted as evidence that we are viewing the bar/bulge at an angle from its major axis and that the closer end of the bar is at positive longitude. There is still disagreement on the parameters of the bar, i.e. its length, strength, pattern speed and position angle. But, if we were to view the Galaxy edge-on from outside, it would probably look much like NGC 891, with probably more bulge than NGC 891 but less than NGC 4565 (see the Hubble Atlas).

2.2. Axisymmetric models

Kent (1992) used infrared ($2.4\mu\text{m}$) surface photometry from the Spacelab infrared telescope to make an axisymmetric model for the luminosity density distribution in the inner galaxy. For the disk, he modelled the luminosity density L as a double exponential in R and z , and for the bulge he adopted

$$L(R, z) = 3.53K_0(s/667) \quad L_\odot \text{ pc}^{-3} \quad \text{for } s > 938$$

and

$$L(R, z) = 1.04 \times 10^6 (s/0.482)^{-1.85} \quad L_\odot \text{ pc}^{-3} \quad \text{for } s < 938.$$

where K_0 is a modified Bessel function. Here $s^4 = R^4 + (z/0.61)^4$ and the units of s in the equation above are parsecs. This form of the $L(R, z)$ distribution for the bulge leads to box-shaped isophotes.

Kuijken (1995) used a quadratic programming technique on a bilinear tessellation in the energy, angular momentum (E, L) plane to construct a two-integral distribution function $f(E, L)$ for a slightly modified version of Kent's axisymmetric model for the inner Galaxy. The distribution function is forced to give an isotropic velocity dispersion. With Kent's values for the mass to light ratios for the disk and bulge, the predicted line-of-sight velocity distribution in Baade's window is in excellent agreement with the distribution

observed for the M giants by Sharples et al. (1990). However, the agreement is not so good for the velocity distribution of the K giants in Minniti’s (1992) field at $l = 8^\circ$, $b = 7^\circ$: the discrepancy between the data and the prediction from the distribution function $f(E, L)$ is seen in the mean velocity and in the shape of the velocity distribution in this region. Kuijken suggests that the discrepancy might be associated with the triaxiality of the bulge, and points out how remarkable it is that his oblate, isotropic and axisymmetric model gives such a good fit to the velocity distribution in Baade’s Window.

Durand et al. (1996) used a two-integral axisymmetric model with a Kuzmin-Kutuzov Stäckel potential (with a halo-disk structure) to study the dynamics of a sample of 673 PNe taken from the Acker et al. (1992) catalogue. The method fits the kinematics to the projected moments of a distribution function by means of Quadratic Programming. They conclude that their two-integral model does not adequately characterize the dynamical state of their sample of PNe.

Our particular interest here is in investigating the triaxial structure of the bar-bulge further, so we will not pursue the axisymmetric models in this paper. The question is about the origin of central bar-bulges: do they arise from instabilities of the disk of galaxies or from other processes like the accretion of satellites or as part of the dissipative collapse of the galaxies ? The quantitative study of the formation of bars through disk instabilities is now well advanced through N-body models, which we now discuss briefly. In §6.3, we will compare the kinematical properties of our PNe and the models. For the N-body models, this comparison will show whether the instability picture gives a plausible description of the observed bulge kinematics.

2.3. N-body models

In the last few years, the growing evidence for a bar at the center of our Galaxy initiated much interest in developing detailed dynamical models of the Galactic bar-bulge. Different kinds of models are now available, but the observational constraints on their stellar dynamics are not yet well advanced.

N-body models of the bar-forming instabilities of disks provide theoretical predictions of the dynamics of the resulting bar-bulges which can be tested against dynamical data from the Galactic bulge and other bulges. For example, Fux (1996), Sellwood (1993) and Kalnajs (1996) have all modelled the central bar-bulge through the instabilities of self-gravitating stellar disks. As tests of the relevance of these models to the dynamics of the Galactic bulge, the detailed kinematics of their models can be compared with the observed kinematics of tracer bulge objects like the PNe which are the subject of this paper.

Another kind of numerical model for the Galactic bulge comes from the work of Zhao (1996) who constructed a rotating Schwarzschild model for the COBE light distribution. Although this model does not provide direct insight into the formation of the bulge, in the way that the studies of disk instabilities can do, the Schwarzschild model is of much interest for evaluating the present dynamical state of the bulge. For this purpose, we can compare the kinematics of N-body realizations of this model with observational data, as above.

It would be most desirable if we could obtain an unbiased spatial distribution and the radial velocities of a subset of bulge objects. Such a database would allow us to distinguish between the various proposed models, and no doubt suggest others. Unfortunately most of the stellar objects have to contend with the high and patchy absorption near the Galactic plane [OH-IR stars are a clear exception].

3. Planetary Nebulæ as tracers

To study the kinematics of the Galactic bulge, we have access to a wide range of tracers: OH/IR stars (Habing 1993; Sevenster et al. 1997a,b), Miras (Whitelock 1993), M giant stars, K giant stars (both individually and through the integrated bulge light) (Walker et al. 1990; Minniti et al. 1992; Minniti 1996a,b; Terndrup 1993; Ibata & Gilmore 1995a,b), carbon stars (Whitelock 1993), SiO Maser sources (Deguchi 1997), RR Lyræ stars (Walker & Terndrup 1991) and PNe (Kinman et al. 1988; Durand et al. 1998). The highly evolved OH/IR stars, Miras and M giants stars are probably biased towards the metal-rich population: the radial distribution of these objects is significantly steeper than the distribution of integrated light in the bulge (e.g. de Zeeuw 1993), and the kinematics of these objects reflects the kinematics of the metal-rich component of the bulge (Sevenster 1997). The carbon stars are rare and are also an indication of an intermediate age metal-rich population. The K giant stars are found at all metallicities and would be the ideal tracers to use since all bulge stars are likely to go through a K giant phase, but they are relatively faint. The K giants have already provided important dynamical information (e.g. Terndrup et al. 1995; Ibata & Gilmore 1995a,b), and much more will appear in the future from the large fiber surveys in progress (e.g. Harding & Morrison 1993). The RR Lyræ stars are also useful bulge tracers but they are biased toward the metal-poor population and are fainter than the K giants. The PNe are not biased towards the metal-rich population (e.g. Hui et al. 1993): recall the presence of PNe in the very metal-poor globular cluster M15 (Pease 1928). Their spatial distribution and their high velocity dispersion indicate that most of the bulge PNe are old objects. Their strong $H\alpha$ and [OIII] emission lines make their velocities easy to measure. We have thus decided to use the PNe as probes to study the kinematics and dynamics of the Galactic bulge.

The distances of PNe are still poorly known. Using the optical diameter as a distance

criterion is not adequate because PNe have a wide range of absolute diameters. Nevertheless, using the angular diameters, spatial distribution and radial velocities of a sample of PNe, Gathier et al. (1983) estimated that probably 80% of the small (diameter $< 20''$) PNe within 10° of the Galactic center belong to the bulge. While it is clear that most of the PNe towards the bulge are associated with the bulge, it is also evident that their apparent spatial distribution at low Galactic latitudes is affected by the interstellar absorption.

3.1. The Data

In 1994 and 1995, we conducted an $H\alpha$ imaging survey of the Galactic bulge in order to detect new PNe (Beaulieu et al. 1999). The survey yield 56 new and 45 already catalogued PNe. We obtained radial velocities for each new PNe plus a sample of 317 catalogued PNe (i.e. 272 catalogued and the 45 rediscovered PNe) taken from the Strasbourg-ESO Catalogue of Galactic Planetary Nebulæ (Acker et al. 1992). Although we intended to observe only the southern part of the bulge (less affected by extinction), we have obtained a few fields in the northern part as well. Our data have already been used in a study of Galactic kinematics by Durand et al. (1998).

Our database of PNe contains two samples. The first sample comprises the 97 PNe (new and rediscovered) found in the southern bulge from our uniform survey with the 1.0m telescope. The region covered by this survey is $-20^\circ < l < 20^\circ$ and $-5^\circ > b > -10^\circ$. We will refer to this uniformly selected sample as the *Survey fields only* sample. A note is needed here: this sample, in fact, contains 98 PNe but we are using 97 PNe for the analysis. The reason for this is that we accepted one PN as “probable” after we have completed the *Survey fields only* sample analysis. This PN is SB15 : PNG009.3 – 06.5.

The second sample is less homogeneous, with the 98 PNe *Survey fields only* sample

(including, this time, *SB15*), the 3 PNe which we discovered in the northern bulge, and the 272 PNe from the Acker et al. (1992) catalogue for which we have measured new radial velocities. This larger sample contains 373 PNe and covers the more extended region $-30^\circ < l < 30^\circ$ and $3.3^\circ < |b| < 15^\circ$. We will refer to this sample as the *Survey fields + Catalogue* sample. Figure 2 shows the (l, b) distributions for the two samples.

In the absence of information on distances for our PNe, we made no attempt to separate disk and bulge PNe in our two samples. Therefore, disk contamination is likely. We note, however, that some of the dynamical models used in this study (see §6) include a disk.

4. Analysis

In the first part of this section, we present several plots showing the kinematics of these two samples for preliminary visual assessment. We then go on to compare the properties of the PNe samples with the properties of several recent dynamical models. This comparison will be first presented visually in the form of plots of individual velocities, mean velocities and velocity dispersions against l and b . Then we will use a statistical technique by Saha (1998) to make a more quantitative comparison of the data with the models, and to estimate the Galactic scaling parameters and orientations which best match the models to our data.

The typical radial velocity error for our PNe is 11 km s^{-1} (Beaulieu et al. 1999). For the Galactic bulge, the velocity dispersion ranges from about 60 km s^{-1} to 125 km s^{-1} (Fig. 13), so this radial velocity error is negligible.

In the presentation of the kinematics of our samples, in order to illustrate the systemic rotational properties of the bulge PNe more clearly, we will show the velocities of the PNe corrected for the solar reflex motion. We adopted the circular velocity of the Local Standard

of Rest (LSR) at the Sun as 220 km s^{-1} (Kerr et al. 1986). For the Sun’s peculiar velocity relative to the LSR we use 16.5 km s^{-1} towards $l = 53^\circ$, $b = 25^\circ$ (e.g. Mihalas & Binney 1981). The corrected line-of-sight ($V_{los,GC}$) velocity (i.e. the line-of-sight velocity in km s^{-1} that would be observed by a stationary observer at the location of the Sun) is then given by

$$V_{los,GC} = V_{obs} + 220 \sin l \cos b + 16.5 [\sin b \sin 25 + \cos b \cos 25 \cos(l - 53)]$$

where V_{obs} is the heliocentric observed line-of-sight velocity in km s^{-1} .

Figure 3 shows the longitude versus velocity diagram for the *Survey fields only* (top panel) and *Survey fields + Catalogue* (lower panel) (corrected for the solar reflex motion).

In the figures that follow, we note that there must be some level of distance bias in our PNe samples. The longitude distribution of the PNe shows some evidence for depletion at $l < 0$ (the more distant side of the bar) relative to $l > 0$ (Fig. 14), although this depletion is only marginally significant (Fig. 16). In the comparisons of the PNe distribution and kinematics with the various models (§6), we will ignore this distance bias.

4.1. Survey fields only

Figure 4 shows the longitude versus mean velocity (top panel) and the longitude versus velocity dispersion (lower panel) using 8 bins in longitude, with approximately equal numbers of PNe in each bin (12 to 13 PNe). The rotation of the bulge is clearly seen, with an amplitude of about $\pm 100 \text{ km s}^{-1}$. The velocity dispersion of the bulge is approximately constant with longitude, except for the apparent drop in σ for $l > +12^\circ$. This drop is seen again in the larger sample described in §4.2 but on both sides of the Galactic center: see Figure 7. It is probably due to the contribution of the inner disk at these longitudes (see Lewis & Freeman 1989).

Figure 5 shows the latitude versus mean velocity (top panel) and the latitude versus velocity dispersion (lower panel) for 2 bins with equal number of PNe in latitude. Each bin in latitude contains 48 to 49 PNe. We see that the *total* velocity dispersion about the mean velocity does not appear to change significantly with latitude. [Note that this total velocity dispersion in the plots against latitude includes the systemic rotation and random velocities of the stars.]

Tables 1 and 2 summarize the binned data shown in Figure 4 and 5 respectively. Column 1: the mean latitude and longitude, Column 2: the mean velocity (km s^{-1}), Column 3: the velocity dispersion, Column 4: the error (standard deviation) in the mean velocity, and Column 5: the error (standard deviation) in the velocity dispersion.

We have also divided the $l - V$ diagram of Figure 3 (top panel) into two bins in Galactic latitude (with 48 to 49 PNe in each bin) (Figure 6) in order to see if contamination from disk PNe is affecting our data. Disk contamination is potentially more serious at higher latitudes because of the steeper density gradient of the bulge. Therefore, if contamination were present, we would expect the lower latitude bin ($b = -04.9^\circ$ to -06.5°) to be significantly hotter (i.e. have higher velocity dispersion) than the higher latitude bin ($b = -06.6^\circ$ to -10.2°). We see no evidence in Figure 6 for serious disk contamination in our sample, except possibly for $l > +12^\circ$.

4.2. Survey fields and Catalogue objects

Now we present the data for the larger and more extended but less homogeneous *Survey fields + Catalogue* sample of 373 PNe. (see Figure 3 (lower panel)). Figure 7 shows the longitude versus mean velocity (top panel) and the longitude versus velocity dispersion (lower panel) using 12 bins in longitude with approximately equal numbers (31 to 32) of

PNe in each bin. Again, the rotation of the bulge is clearly seen. For $|l| > 12^\circ$, the mean rotational velocity continues to rise as the data become dominated by PNe of the inner disk. In this larger sample, beyond $|l| > 12^\circ$, we see again an apparent drop in the velocity dispersion, due presumably to the contribution of the inner disk PNe at these longitudes.

Figure 8 shows the latitude versus mean velocity (top panel) and the latitude versus *total* velocity dispersion (lower panel) using 6 bins in latitude with approximately equal numbers (62 to 63) of PNe in each bin; 2 bins are in the northern bulge and 4 bins in the southern bulge. [Note again that the total velocity dispersion in the latitude plots includes the systemic rotation and random velocities of the stars.]

Tables 3 and 4 summarize the binned data shown in Figure 7 and 8 respectively. Column 1: the mean latitude and longitude, Column 2: the mean velocity (km s^{-1}), Column 3: the velocity dispersion, Column 4: the error (standard deviation) in the mean velocity and Column 5: the error (standard deviation) in the velocity dispersion.

In Figure 9, we are looking again at the disk contamination using the same latitude bins as for the *Survey fields only* sample. In this larger and more extended sample, contamination from the disk PNe becomes evident outside the longitude region $|l| = 12^\circ$ where the PNe velocity distribution becomes significantly colder.

We also present a series of longitude-velocity diagrams for 6 bins in latitude. Figure 10: $b = +03.3^\circ$ to $+05.2^\circ$ (top panel) and $b = +05.2^\circ$ to $+15.1^\circ$ (lower panel). Figure 11: $b = -03.3^\circ$ to -04.4° (top panel) and $b = -04.5^\circ$ to -05.8° (lower panel). Figure 12: $b = -05.8^\circ$ to -07.4° (top panel) and $b = -07.4^\circ$ to -14.9° (lower panel). For this less homogeneous (and generally brighter) sample of PNe, the disk contamination really starts to show in the two high latitude bins: the PNe velocity dispersion becomes much colder at all longitudes, as we would expect to see if the disk contamination is significant at higher latitudes.

4.3. Comparison with other studies

In recent years, there have been some important studies of the kinematics of K and M giants in the Galactic bulge. Although the regions observed are mostly not as extended as our survey, we should now compare the kinematics derived from these studies with the results from the PNe.

In Figure 13, we show again the mean velocity and velocity dispersion against longitude for our extended sample, and have overplotted data from kinematic studies of giants, which fall in our *Survey fields + Catalogue* sample region. Minniti (1996a) presented data for three bulge fields. He gives kinematical data for the more metal-rich ($[\text{Fe}/\text{H}] > -1$: filled symbols) and metal-poor stars ($[\text{Fe}/\text{H}] < -1$: open symbols) separately. Data for one field come from Harding and Morrison (1993), and again we show the data points for the more metal-rich and more metal-poor stars separately. For Baade’s Window (K giants: Terndrup et al. 1995), we show the only available data point, the velocity dispersion value, for his stars with $V \geq 16.0$: these fainter stars are likely to be a relatively uncontaminated sample of bulge stars. Sharples et al. (1990) find an almost identical dispersion for their M giants in Baade’s Window. Finally, we present three data points (higher latitude [$b = -12^\circ$]) from Ibata & Gilmore (1995a,b). We derived equivalent $\langle V_{los,GC} \rangle$ values for their three negative longitude fields from the gradients Ω_G that they estimated assuming an isotropic velocity dispersion. We used the formalism of Morrison et al. (1990), assuming that the stars in each field lie where the line-of-sight passes closest to the center of the bulge. Ibata and Gilmore give kinematical solutions for several assumptions about the shape of the bulge velocity ellipsoid σ . The derived $\langle V_{los,GC} \rangle$ values depend very weakly on the assumptions about the shape of σ , so we have only plotted the isotropic solution (asterisks) in Figure 13 (upper panel). Their velocity dispersions are more sensitive to the shape of σ . We show their velocity dispersions for an isotropic bulge (asterisks) in Figure 13 (lower

panel). The isotropic solution for σ appears to give better agreement of the Ibata and Gilmore data with the other bulge samples. For comparison we also show (line) the slope of the linear rotation curve found for 279 bulge PNe by Durand et al. (1998). (Part of our data is included in their analysis.) The slope of this line is $9.9 \text{ km s}^{-1} \text{ degree}^{-1}$. Table 5 summarizes the symbols associated with each study. Column 1: the study, Column 2: the field’s (l, b) coordinates, and Column 3: the symbol used on the plot.

For Minniti’s three fields, the data for the metal-rich giants clearly matches our PNe data better than do the metal-poor giants. For the Harding-Morrison field, although we see the same match of the metal-rich giants with our PNe in the velocity dispersion, it is in fact the opposite that is seen for the mean velocity. This disagreement was also observed by de Zeeuw (1993) when he compared the Minniti and Harding-Morrison samples with Kent’s model (Kent 1992). Nevertheless, the otherwise good agreement seen so far identifies the bulge PNe with the more metal-rich giant ($[\text{Fe}/\text{H}] > -1$) of the bulge, as we would expect. For Baade’s Window, it is interesting to see that the velocity dispersion is perhaps somewhat higher than the mean of the velocity dispersion values for our PNe at lower $|l|$, but we note that our PNe are mostly more distant from the Galactic plane than Baade’s Window (cf Figure 8). (The velocity dispersion along the minor axis of the Galactic bulge is known to decrease with increasing $|b| \gtrsim 2^\circ$: e.g. Rich 1996.)

We note that the $\langle V_{los,GC} \rangle$ values shown in Figure 13 for the Ibata and Gilmore sample pertain to their more metal-poor stars with $[\text{Fe}/\text{H}] < -0.5$. The shallower slope of the $\langle V_{los,GC} \rangle - l$ relation for their stars is consistent with the metallicity trends seen in the Minniti and Harding-Morrison samples.

5. Comparison with COBE images

The COBE/DIRBE images in the 1.25, 2.2 and 3.5 μm wavelength regions allow us to compare the distribution of the PNe with the integrated near-infrared emission from the Galactic bulge. In this region of the spectrum, the light distribution comes from various stellar populations but is dominated by the more metal-rich K and M-giants which have kinematics similar to those of the PNe. The 1.25 μm map also gives an indication of the distribution of the dust.

5.1. Histogram of the Longitude Distributions

Figure 14 shows a histogram of the longitude distribution of the COBE light and the PNe in our southern surveyed fields ($-5^\circ > b > -10^\circ$). The COBE histograms were constructed from the COBE light distribution within the individual 30 arcmin fields used for the PNe survey (see Beaulieu et al. 1999), so the distributions are directly comparable. The dashed lines represent the three bands (1.25, 2.2 and 3.5 μm) of the COBE light distribution and the solid line represents the PNe distribution. We see immediately that the three COBE distributions agree very well and that the PNe distribution follows the COBE light distribution. The fact that the three COBE light distributions agree so well is an indication that extinction, in our surveyed fields, is not severe and that its distribution is fairly uniform.

We also compare the three COBE light distributions with their cumulative distributions, in preparation for the next section. Figure 15 shows that the cumulative distributions for the three COBE bands are very similar.

5.2. K-S Test

The Kolmogorov-Smirnov (K-S) test estimates the probability that a set of observed values can be excluded as coming from a given specified distribution.

We performed a one-sample, two-tailed K-S test in our surveyed fields (Galactic longitude $l = +20^\circ$ to -20° and Galactic latitude $b = -5^\circ$ to -10°) using the well-determined COBE light distribution in longitude as the specified distribution and our sample of PNe as the observed distribution. The test uses the largest value D of the deviation $|F_0(X) - S_N(X)|$ where $|F_0(X)$ and $S_N(X)|$ are the cumulative distributions of the specified distribution (the COBE light distribution) and the set of observed values (the longitude distribution of our PNe counts). We have seen in Figure 15 that the cumulative distributions of the three COBE colors agree very well and the results for the maximum deviation will be similar in all three colors.

Figure 16 shows the two cumulative distributions for our PNe sample and the $2.2\mu\text{m}$ COBE light. The ordinate, N , has been normalized to 1.0 for both distributions. We have used table E of Siegel (1956) to estimate the probabilities. Table 6 gives the results obtained for the maximum deviation D and the associated probability that the deviation D could occur by chance from the same parent distribution. Column 1: the COBE band, Column 2: the maximum deviation value D and and Column 3: the associated probability of occurrence. This probability is between 0.23 and 0.30, and we conclude that there is no significant difference between the longitude distribution of the PNe and the COBE light in the zone of our deep survey.

6. Comparison with models

The evidence for a bar in our Galaxy initiated much interest in developing detailed dynamical models (N-body and Schwarzschild) of the Galactic bar-bulge. Several different kinds of models are now available, but the observational constraints on their stellar dynamics are still weak. Our kinematical data for the PNe of the Galactic bar-bulge provide further constraints on the models.

In this section, we present the data of our survey with velocities relative to the LSR, using the parameters for the sun’s peculiar motion as given in the equation in §4. The motivation for doing so is that most observational studies are presented in that manner and it would therefore be easier for future comparison. Also, we will use our data to estimate the best value of the tangential velocity of the LSR for each model.

6.1. Presentation of the models

At the time of conducting this study, there were four triaxial numerical models available to study the dynamics of the Galactic bulge. They offer interesting and different approaches to studying the formation and structure of the bar-bulge. There are three N-body models (Sellwood 1993; Fux 1996; Kalnajs 1996) and one Schwarzschild model with an N-body realization (Zhao 1996). (Very recently, a more elaborate Schwarzschild model has appeared (Häfner et al. 1999), constrained by a subset of the data in Figure 13 plus some proper motions.)

6.1.1. *Sellwood's model*

Sellwood's model is one of the earlier N-body dynamical models. It is a purely stellar N-body system with 5×10^4 particles. It starts from a $Q = 1.2$ axisymmetric Kuz'min-Toomre disk which contains 70% of the total mass. The remaining 30% is in a rigid Plummer sphere which has half the scale length of the disk. The bar-bulge forms through the instability of the disk. The resulting model shows a peanut-shaped bulge. At a viewing angle of 30° to the major axis and a finite distance from the center, the model shows an asymmetry in longitude between the positive and negative sides, which is consistent with the one seen in the COBE/DIRBE image (Weiland et al. 1994).

Figure 17 presents the face-on view (XY) and the edge-on view (YZ) as seen from infinity, with the Sun-center line at an angle of 30° from the major axis.

6.1.2. *Fux's model*

Fux's model is an N-body system of stars. It has four components: an exponential stellar disk of constant thickness (15×10^5 particles), a composite power-law stellar nucleus-spheroid (5×10^4 particles), a dark halo (2×10^5 particles), and a dissipative gas component (a smoothly truncated Mestel disk with 2×10^4 particles). The system starts in equilibrium and the rotating bar forms through instabilities. The model provided to us by Fux is a gas-free version which has evolved for 5 Gyr: we note that Fux (1997) has built more elaborate models of the Milky Way including gas, which we have not considered here.

Figure 18 presents the face-on view (XY) and the edge-on view (YZ) as seen from infinity, with the Sun-center line at an angle of 30° from the major axis.

6.1.3. *Kalnajs' model*

Kalnajs has been conducting numerical experiments on thin self-gravitating disks which turn into triaxial rotating objects because of buckling instabilities. The projected shapes of these objects, when viewed from the right distance and orientation, resemble the light distribution of the Galactic bulge, and the line-of-sight velocities can be scaled to match observed motions of planetary nebulae in the bulge. The experiments use only 8000 particles, but since the triaxial objects appear to be stationary in a rotating frame, one can add the distributions at different times and obtain models containing effectively $\approx 10^5$ particles.

Figure 19 presents the face-on view (XY) and edge-on view (YZ) as seen from infinity, with the Sun-center line at an angle of 45° from the major axis.

6.1.4. *Zhao's model*

The last is a model of the COBE bar, constructed from 10K orbits (direct, retrograde and chaotic) in the rotating bar potential plus a rigid Miyamoto-Nagai disk potential, using the non-negative least square fitting technique pioneered by Schwarzschild.

The model provided by Zhao for our comparison is the system allowed to evolve as an N-body system after 10 rotations and it contains 32634 particles.

Figure 20 presents the face-on view (XY) and the edge-on view (YZ) as seen from infinity, with the Sun-center line at an angle of 20° from the major axis..

Table 7 summarizes the parameters suggested by the authors of each model. Column 1: the model, Column 2: the total number of particles in the model, Column 3: the solar galactocentric radius R_\odot (in model units), Column 4: the viewing angle ϕ (in degrees) of

the bar. ϕ is the angle between the major axis of the bar and the Sun-center line, and is taken as positive for a bar pointing into the first quadrant of l, Column 5: the velocity scale V_{scale} (km s^{-1} per model unit) of the model, and Column 6: the solar tangential velocity $V_{o,T}$ (km s^{-1}).

In the next section, we use a statistical technique to estimate these scaling parameters for each model from our data.

6.2. Search for best parameters

The authors of each model have suggested values for the Sun’s galactocentric distance (in model units), the viewing angle of the bar and a velocity scale (Table 7). However, by varying these parameters, we may hope to obtain somewhat better fits to the present data. There are four parameters one can vary: (i) the overall spatial scale of the model, or equivalently R_0 in model units; (ii) the overall velocity scale; (iii) the viewing angle of the bar; and (iv) the tangential velocity of the LSR. Saha (1998) has developed a method for searching the space of these four parameters for values which are most likely to have given rise to the observed data. We used his code, which gives a median fit for the four parameters and error bar estimates under the assumption that the models and the data are drawn from the same underlying distribution function.

We are going to compare the positions and the radial velocities of the 97 PNe from the *Survey fields only* sample with those of the four models. We choose to restrict the comparison to the 97 PNe in our survey region, because they were selected in a homogeneous manner. In making our comparison we must only use that part of the model which would fall into our surveyed window. Since our window lies several scale lengths below the Galactic plane, only a small fraction of the model particles are used in the comparison. The number

of model particles is held fixed as the observer’s position changes: the respective numbers for Sellwood, Fux, Kalnajs and Zhao were 400, 6000, 9000 and 1700.

We use Saha’s procedure to make a quantitative comparison of the (l, b, V_{los}) distributions for samples of observed objects and N-body models. Saha’s statistic is

$$W = \prod_{i=1}^B \frac{(m_i + s_i)!}{m_i! s_i!}$$

where the (l, b, V_{los}) space has been partitioned into a total of B cells, m_i and s_i are the numbers of model and sample objects in the i -th cell; W is proportional to the probability that both the observed sample and the model come from the same underlying (but unknown) distribution, so W can be used to compare the goodness of fit of various models. As described above, the W statistic also serves to estimate the scaling parameters for each model from the observed sample. (see Sevenster et al. 1999 for a previous application of this statistic.)

For choosing the number B of cells, our guideline is that the average number of model particles per cell should be 5 or more, and the spatial cells should not be smaller than important features in the distribution function, such as the scale height (see Saha 1998 for more discussion). After some experimentations, we used a total of 260 cells in (l, b, V_{los}) : 13 in l , 2 in b and 10 in V_{los} . Table 8 presents the results: Column 1: the model, Column 2: the total number of particles in our window, Columns 3: the four parameters (i) the solar orbit radius R_o in model units, (ii) the orientation angle ϕ in degrees, (iii) the velocity scale (in km s^{-1} per model unit), and (iv) the solar tangential velocity (in km s^{-1}), Column 4: give the median and the 90 % confidence limits for these parameters.

These results are produced by the program after searching through the region of parameter space given by $7 < R_o < 9$, $0^\circ < \phi < 90^\circ$, $200 < V_{o,T} < 240$ and

$0 < V_{scale}/V_{scale,model} < 2$, where $V_{scale,model}$ is the suggested velocity scale value from each model (see table 7). This choice of search region was partly guided by the likely values of the corresponding galactic parameters and appears to be satisfactory: for every parameter and every model, the median estimate of the parameter lies away from the boundary of the search region by at least the 90% confidence limit. Of these parameters, V_{scale} is the least constrained by the data, and $V_{o,T}$ the best constrained. For all of the models, the W statistic indicates that the probability that the models and data come from the same underlying distribution exceeds 98%.

6.3. Models versus Data

With the estimated parameters given in Table 8, we now present some visual comparisons of the kinematics of the models and the data. The figures are similar to those shown earlier for our data alone, except for the fact that the PNe velocities and the velocity data for the models are heliocentric.

Figures 21 to 24 present the longitude-velocity diagrams for Sellwood (400 particles), Fux (6000 particles), Kalnajs (9000 particles) and Zhao (1700 particles) respectively.

Figures 25 to 28 show $\langle V_{los} \rangle$ (top panel) and σ (lower panel) against the longitude for the data and models, with the model represented by thick lines.

The main features of the $(\langle V_{los} \rangle, \sigma)$ versus longitude relations are that all models give a fair representation of the observed $\langle V_{los} \rangle - l$ distribution, but the Sellwood and Zhao models have a velocity dispersion that is relatively low. The V/σ values for the Sellwood and Zhao models appear to be somewhat higher than for the bulge of the Galaxy, at least in the region of our survey. But, as indicated by the Saha procedure, all of the models are good representations of the PNe data.

6.4. Models versus Models

We attempted to use the program to discriminate between the models by intercomparing the maximum W value from Saha’s procedure for samples of similar total numbers of particles. For example, Sellwood’s model has 400 particles in our survey region, so we estimated values of W for Sellwood’s model and random samples of 400 particles drawn from the larger simulations (Zhao, Fux, Kalnajs) within our region. Similarly, Zhao’s model has 1700 particles within our region, so we compared W values for Zhao’s model and random samples of 1700 particles from the larger simulations (Fux, Kalnajs). Table 9 presents values of $\ln W$ for each set of comparisons.

The total number of particles is shown for each comparison. The sampling standard deviation of $\ln W$ is derived empirically by the program. Table 9 shows: Column 1: the models being compared and Column 2: the value of $\ln W$ for each set of comparisons, i.e. 400, 1700 and 6000 particles. The last line of Table 9 shows the sampling standard deviation of $\ln W$ of each run. We recall that for all of the models, the probability that the models and the data come from the same underlying distribution is more than 98 %.

We see that the values of $\ln W$ for each model do not differ by more than about 1.9σ , indicating again that there is no significant difference between the ability of the various N-body models to represent our data. Table 9 shows that Sellwood’s model comes out best in the N=400 comparison of the four models, despite the apparently large deviations in the velocity dispersion (Figure 25). We recall that the W -statistic involves comparison of data and model over cells in velocity *and* (l, b) . The quality of the velocity comparisons is seen in Figures 25-28. Figure 29 shows the cumulative distributions over l of the four models (all with N=400) and the survey fields only PNe sample (over the same interval in b). Sellwood’s model lies closest to the data in Figure 29, followed by Zhao’s model. This help to understand the ordering of the $\ln W$ values for the models as given in Table 9.

7. Summary and Conclusions

Planetary Nebulæ are good tracers for a dynamical study of the Galactic bulge because they are less affected by metallicity bias than most other tracers and they are strong emitters in $H\alpha$ - this makes their velocities easy to measure. We chose to survey the southern Galactic bulge in the region $l = \pm 20^\circ$ and $b = -5^\circ$ to -10° because of its lower extinction relative to the northern bulge.

We compared the longitude distribution of PNe in our surveyed fields with the COBE light distribution at 1.25, 2.2 and $3.5\mu\text{m}$. We conclude that (i) the light distributions in the three COBE bands agree very well, indicating that the extinction in our surveyed fields is not severe and that its distribution is fairly uniform and, (ii) there is no significant difference between the longitude distribution of the PNe and the COBE light in the zone of our deep survey.

Recent studies of stellar kinematics in a few clear windows in the Galactic bulge have provided mean velocities and velocity dispersions which can be compared with our data. We thus compared data from Minniti (1996a), Harding and Morrison (1993), Terndrup et al. (1995) and Ibata and Gilmore (1995a,b), and found that the metal-rich stars in Minniti's three fields agree very well with our data. Harding and Morrison's metal-rich stars agree well with our velocity dispersion data for the PNe, but not so well with our mean velocity. We also found that the velocity dispersion in Baade's Window (Terndrup et al. 1995) is somewhat higher than ours near $l = 0$ but note that Baade's window is closer to the Galactic plane than most of our PNe. For the Ibata and Gilmore data, the velocity gradient over l is shallower than for the PNe and other samples of giants; this is presumably due to their restriction to more metal-weak giants ($[\text{Fe}/\text{H}] < -0.5$). Their velocity dispersion estimates for an isotropic bulge agree better with the PNe values.

To assist in the comparison of the four N-body models with our sample of data, we used

a procedure proposed by Saha (1998) to make a quantitative comparison of the (l, b, V_{los}) distributions for samples of observed objects and N-body models. The main conclusion from this comparison is that all four models show a fairly good fit to our data.

Sellwood, Fux and Kalnajs’ models are all bar-forming systems via the instabilities of a disk and, after scaling, are kinematically more or less similar. Zhao’s model is constructed to fit the COBE light: in this sense, it is a step up from Kent’s (1992) axisymmetric model for the Spacelab near-IR photometry. Kent’s predicted velocity dispersion, as quoted by de Zeeuw (1993), was already a fairly good fit to the existing data; therefore, it is not surprising that Zhao’s model should also fit well.

Using the estimated parameters obtained from Saha’s procedure, we made some visual comparisons of the kinematics of the models and the data. The Kalnajs and Fux models give a good visual representation of the mean velocity and velocity dispersion of the bulge in our survey region; the Sellwood and Zhao models represent the mean velocity well but their velocity dispersion is marginally low relative to the PNe observations.

It will be interesting to use our PNe sample as a more detailed kinematical test of Kuijken’s axisymmetric isotropic two-integral model. One important goal of this comparison would be to look for kinematical disagreements between the data and the axisymmetric model that might be kinematical signatures of triaxiality. In the same spirit, it would be interesting to compare Kuijken’s model in detail with the numerical triaxial systems discussed in §6.

We saw earlier that Minniti’s data (Minniti et al. 1992) is apparently not consistent with Kuijken’s model. As a preliminary comparison with Kuijken’s model, we examined the distribution of LSR velocities for our *Survey fields + Catalogue* sample. Figure 30 shows a histogram of LSR velocities for the PNe with $5^\circ < l < 10^\circ$. We can compare the velocity distribution in the region $5^\circ < l < 10^\circ$ with the distribution measured by Minniti

et al (1992) for the giants towards $l = 8^\circ, b = 7^\circ$ and discussed by Kuijken (1995). The PNe in our $5^\circ < l < 10^\circ$ region cover a larger region of sky than the Minniti sample; however, the mean value of $|b|$ for the PNe is about 6° , so we might expect the velocity distributions of the PNe and the giants to be at least qualitatively similar. We see from Figure 30 that the velocity distribution in the region $5^\circ < l < 10^\circ$ is asymmetric; the asymmetry is in the opposite sense to that found by Minniti et al. (1992) but closer to that seen for the more metal-rich stars in Minniti’s later (1996b) study for this field. The mean LSR velocity for our sample is $36 \pm 11 \text{ km s}^{-1}$, compared with $5 \pm 10 \text{ km s}^{-1}$ for the Minniti et al. (1992) sample and the predicted value of 32 km s^{-1} for the Kuijken model. There seems to be better agreement between the PNe and the two-integral model in this region than was found between the model and the giants.

It may be that we are seeing an effect of metallicity in the Minniti et al. (1992) sample. There was no information about metallicity at that time so the sample could be suffering from pollution by the more slowly rotating metal-poor stars. We recall here that the metal-rich stars in Minniti’s three fields (Minniti 1996a) are in good agreement with our *Survey fields + Catalogue* sample (cf Figure 13).

So far, only a few clear Galactic bulge windows have been extensively studied. Although these studies provide important information on the kinematics in the bulge, their small region do not give us the entire picture of the bulge kinematics. Two major studies of tracers in the Galactic bulge, the K giants (Harding & Morrison 1993) and the OH/IR stars (Sevenster et al. 1997a,b) and a new PNe $H\alpha$ survey of the Southern Galactic Plane (Parker & Phillips 1998) are presently under way. A comparison of the PNe surveys with the results coming from the OH/IR and K giants large-scale surveys should clearly indicate any dynamical differences between the populations from which these different tracers come.

Finally, we conclude that the existing studies give a more or less consistent picture of

the kinematics of the Galactic bulge, as summarized in Figure 13, at least for the metal-rich bulge tracers. We find it interesting that the N-body models, in which the bar/bulge grows from the disk via bar-forming instabilities, give a good representation of the detailed stellar kinematics of the bulge.

SFB wish to acknowledge funding from The Australian Government through an Australian National University Scholarship and an Overseas Postgraduate Research Scholarship. We are most grateful to Roger Fux and Jerry Sellwood for allowing us to use their models. Our thanks go to Gerry Gilmore for critical comments on the manuscript.

REFERENCES

- Acker, A., Ochsenbein, F., Stenholm, B., Tylenda, R., Marcout, J. & Schohn, C. 1992, in
The Strasbourg-ESO Catalogue of Galactic Planetary Nebulæ, (Germany:ESO)
- Arendt, R. G., Berriman, G. B., Boggess, N., Dwek, E., Hauser, M. G., Kelsall, T., Moseley,
S. H., Murdock, T. L., Odegard, N., Silverberg, R. F., Sodroski, T. J. & Weiland, J.
L. 1994, *ApJ*, 425, L85
- Beaulieu, S. F., Dopita, M. A. & Freeman, K. C. 1999, *ApJ*, 515, 610
- Binney, J. & Petrou, M. 1985, *MNRAS*, 214, 449
- Binney, J., Gerhard, O. E., Stark, A. A., Bally, J. & Uchida, K. I. 1991, *MNRAS*, 252, 210
- Binney, J., Gerhard, O. & Spergel, D. 1997, *MNRAS*, 288, 365
- Blitz, L. & Spergel, D. N. 1991, *ApJ*, 379, 631
- Bureau, M. & Freeman, K. C. 1999, *AJ*, in press
- Combes, F., Debbasch, F., Friedli, D & Pfenniger, D. 1990, *A&A*, 233, 82
- Deguchi, S. 1997, *IAU Symp.* 184, *The Central Regions of the Galaxy and Galaxies*, ed. Y.
Sofue (Dordrecht:Kluwer), 25
- de Vaucouleur, G. 1964, *IAU Symp.* 20, *The Galaxy and the Magellanic Clouds*, ed. F. J.
Kerr & A. W. Rodgers (Sydney : Australian Academy of Science), 195
- de Zeeuw, T. 1993, *IAU Symp.* 153, *Galactic Bulges*, ed. H. Dejonghe & H. J. Habing
(Dordrecht:Kluwer), 191
- Durand, S., Dejonghe, H & Acker, A. 1996, *A&A*, 310, 97
- Durand, S., Acker, A. & Zijlstra, A. 1998, *A&AS*, 132, 13
- Englmaier, P. & Gerhard, O. 1999, *MNRAS*, 304, 512

- Freeman, K. C. 1996, ASP Conf. Ser. 92, Formation of the Galactic Halo... Inside and Out, ed. A. Sarajedini and H. Morrison, (San Francisco:ASP), 3
- Fux, R. 1996, IAU Symp. 169, Unsolved problems of the Milky Way, ed. L. Blitz & P. Teuben, (Dordrecht:Kluwer), 125
- Fux, R. 1997, A&A, 327, 983
- Fux, R. 1999, A&A, 345, 787
- Gathier, R., Pottasch, S. R., Goss, W. W. & van Gorkom, J. H. 1983, A&A, 128, 325
- Gerhard, O. E. 1999, ASP Conf. Ser. 182, Galaxy Dynamics, ed. D. Merritt, J. A. Sellwood & M. Valluri (San Francisco:ASP), 307
- Habing, H. J. 1993, IAU Symp. 153, Galactic Bulges, ed. H. Dejonghe & H. J. Habing (Dordrecht:Kluwer), 57
- Häfner, R., Evans, N. W., Dehnen, W. & Binney, J., MNRAS, submitted (astro-ph/9905086)
- Harding P. & Morrison, H. 1993, IAU Symp. 153, Galactic Bulges, ed. H. Dejonghe & H. J. Habing (Dordrecht:Kluwer), 297
- Hui, X., Ford, H. C., Ciardullo, R. & Jacoby, G. H. 1993, ApJ, 414, 463
- Ibata, R. A. & Gilmore, G. F. 1995a, MNRAS, 275, 591
- Ibata, R. A. & Gilmore, G. F. 1995b, MNRAS, 275, 605
- Jenkins, A. & Binney, J. 1994, MNRAS, 270, 703
- Kalnajns, A. J. 1996, Nobel Symposium 98, Barred Galaxies and Circumnuclear Activity, Ed. Aa. Sandqvist & P. O. Lindblad (Berlin:Springer), 165
- Kent, S. M. 1992, ApJ, 387, 181
- Kerr, F. J. & Lynden-Bell, D. 1986, MNRAS, 221,1023
- Kinman, T. D., Feast, M. W. & Lasker, B. M. 1988, AJ, 95, 804

- Kochanek, C. S. 1996, ApJ, 457, 228
- Kormendy, J. 1993, IAU Symp. 153, Galactic Bulges, ed. H. Dejonghe & H.J. Habing
(Dordrecht:Kluwer), 209
- Kormendy, J. & Illingworth, G. 1982, ApJ, 256, 460
- Kuijken, K. 1995, ApJ, 446, 194
- Kuijken, K. & Merrifield, M. R. 1995, ApJ, 443, L13
- Lewis, J.R. & Freeman, K.C. 1989, AJ, 97, 139
- Madsen, C. & Laustsen, S. 1986, The Messenger, 46, 12
- Matsumoto, T., Hayakawa, S., Koizumi, H., Murakami, H., Uyama, K., Yamagami, T. &
Thomas, J. A. 1982, The Galactic Center, ed. G. Riegler & R. Blandford, (New
York:AIP), 48
- Mihalas, D. & Binney, J. 1981, Galactic Astronomy: Structure and Kinematics, Second ed.
(San Francisco:W.H. Freeman and Company), 400
- Minniti, D. 1996a, ApJ, 459, 175
- Minniti, D. 1996b, ApJ, 459, 579
- Minniti, D., White, S. D. M., Olszewski, E. W. & Hill, J.M. 1992, ApJ, 393, L47
- Morrison, H. L., Flynn, C. & Freeman, K. C. 1990, AJ, 100, 1191
- Nikolaev, S. & Weinberg, M.D. 1997, ApJ, 487, 885
- Parker, Q. A. & Phillips, S. 1998, PASA, 15, 28
- Pease, F.G. 1928, PASP, 40, 342
- Pfenniger, D. & Friedli, D. 1991, A&A, 252, 75
- Rich, R. M. 1996, ASP Conf. Ser. 92, Formation of the Galactic Halo...inside and out, ed.
H. Morrison & A. Sarajedini (San Francisco:ASP), 24

- Rohlfs, K. & Kampmann, H. 1993, Back to the Galaxy, ed. S. S. Holt & F. Verter, AIP Conf. Proc. 278 (New York:AIP), 122
- Rowley, G. 1986, Ph.D. Thesis, Australian National University
- Saha, P. 1998, AJ, 115, 1206
- Sellwood, J. A. 1993, Back to the Galaxy, ed. S. S. Holt & F. Verter, AIP Conf. Proc. 278 (AIP : New York), 133
- Sellwood, J. A. & Wilkinson, A. 1993, Rep. Prog. Phys., 56, 173
- Sevenster, M. N. 1997, Ph.D. thesis, Sterrewacht Leiden
- Sevenster, M. N., Chapman, J. M., Habing, H. J., Killeen, N. E. B. & Lindqvist, M. 1997a, A&AS, 122, 79
- Sevenster, M. N., Chapman, J. M., Habing, H. J., Killeen, N. E. B. & Lindqvist, M. 1997b, A&AS, 124, 509
- Sevenster, M., Saha, P., Valls-Gabaud, D. & Fux, R. 1999, MNRAS, 307, 584
- Sharples, R., Walker, A., Cropper, M. 1990, MNRAS, 246, 54
- Shaw, M. 1993, MNRAS, 261, 718
- Siegel, S. 1956, Nonparametric Statistics for the behavioral sciences, International Student Edition, (Tokyo:McGraw-Hill Kogakusha), 47
- Stanek, K. Z., Mateo, M., Udalski, A., Szymanski, M., Kaluzny, J. & Kubiak, M. 1994, ApJ, 429, L73
- Terndrup, D. M. 1993, IAU Symp. 153, Galactic Bulges, ed. by H. Dejonghe & H. J. Habing (Dordrecht:Kluwer), 87
- Terndrup, D. M., Sadler, E. M. & Rich, R. M. 1995, AJ, 110, 1774
- Unavane, M., Wyse, R. F. G. & Gilmore, G. 1996, MNRAS, 278, 727

- Walker, A., Sharples, R. & Cropper, M. 1990, *Bulges of Galaxies*, ESO Conference & Workshop Proc. 35, ed. B. J. Jarvis & D. M. Terndrup, (Germany:ESO), 99
- Walker, A. R. & Terndrup, D. M. 1991, *ApJ*, 378, 119
- Weiland, J. L., Arendt, R. G., Berriman, G. B., Dwek, E., Freudenreich, H. T., Hauser, M. G., Kelsall, T., Lisse, C. M., Mitra, M., Moseley, S. H., Odegard, N. P., Silverberg, R. F., Sodroski, T. J., Spiesman, W. J. & Stemwedel, S. W. 1994, *ApJ*, 425, L81
- Weiner, B. J. & Sellwood, J. A. 1999, *ApJ*, 524, 112
- Whitelock, P. 1993, *IAU Symp. 153, Galactic Bulges*, ed. by H. Dejonghe & H. J. Habing (Dordrecht:Kluwer), 39
- Whitmore, B. C. & Bell, M. 1988, *ApJ*, 324, 74
- Wyse, R. F. G., Gilmore, G. & Franx, M. 1997, *ARA&A*, 35, 637
- Zhao, H. S. 1996, *MNRAS*, 283, 149

Fig. 1.— Contours of the COBE/DIRBE $2.2\mu\text{m}$ image.

Fig. 2.— (l, b) distributions for the Survey fields only sample (top panel) and the Survey fields + Catalogue sample (lower panel).

Fig. 3.— Longitude-galactocentric velocity diagram for PNe in the Survey fields only (top panel) and the Survey fields + Catalogue sample (lower panel).

Fig. 4.— Mean galactocentric velocities V (top panel) and velocity dispersions σ (lower panel), versus longitude for PNe in the Survey fields only. We used 8 bins of equal number of PNe. Each bin contains 12 to 13 PNe.

Fig. 5.— Mean galactocentric velocities V (top panel) and velocity dispersions σ (lower panel), versus latitude, using 2 bins of equal number of PNe in the Survey fields only. Each bin contains 48 to 49 PNe.

Fig. 6.— Longitude-galactocentric velocity diagrams for PNe in the Survey fields only. The top panel is for the bin in latitude from -04.9° to -06.5° and the lower panel is for the bin in latitude from -06.6° to -10.2° . Each bin has 48 to 49 PNe.

Fig. 7.— Mean galactocentric velocities V (top panel) and velocity dispersions σ (lower panel), versus longitude for PNe in the Survey fields + Catalogue sample. We used 12 bins of equal number of PNe. Each bin contains 31 to 32 PNe.

Fig. 8.— Mean galactocentric velocities V (top panel) and velocity dispersions σ (lower panel), versus latitude, using 6 bins of equal number of PNe in the Survey fields + Catalogue sample. Each bin contains 62 to 63 PNe.

Fig. 9.— Longitude-galactocentric velocity diagrams for PNe in the Survey fields + Catalogue sample. The top panel is for the bin in latitude from -04.9° to -06.5° and the lower panel is for the bin in latitude from -06.6° to -10.2° . The lower latitude bin (b

= -04.9° to -06.5°) contains 66 PNe and the higher latitude bin contains 73 PNe.

Fig. 10.— Longitude-galactocentric velocity diagrams for PNe in the Survey fields + Catalogue sample. The top panel is for the bin in latitude from $+03.3^\circ$ to $+05.2^\circ$ and the lower panel is for the bin in latitude from $+05.2^\circ$ to $+15.1^\circ$. The bins contains 62 and 63 PNe respectively.

Fig. 11.— Longitude-galactocentric velocity diagrams for PNe in the Survey fields + Catalogue sample. The top panel is for the bin in latitude from -03.3° to -04.4° and the lower panel is for the bin in latitude from -04.5° to -05.8° . Each bin contains 62 PNe.

Fig. 12.— Longitude-galactocentric velocity diagrams for PNe in the Survey fields + Catalogue sample. The top panel is for the bin in latitude from -05.8° to -07.4° and the lower panel is for the bin in latitude from -07.4° to -14.9° . The bins contains 62 PNe.

Fig. 13.— Mean galactocentric velocities V (top panel) and velocity dispersions σ (lower panel), versus longitude for PNe in the Survey fields + Catalogue sample. We used 12 bins of equal number of PNe. Overplotted are data points from four studies of K-giants: filled symbols for metal-rich stars and open symbols for metal-poor stars. *Circle, star and triangle*: Minniti (1996); *diamond*: Harding & Morrison (1993); *filled square*: Terndrup (1995); and *asterisks*: Ibata & Gilmore (1995a,b). The line represents the slope of the linear rotation curve found for bulge PNe by Durand et al. (1998) (part of our data is included in their analysis). More details can be found in Table 5.

Fig. 14.— Longitude distribution of the COBE light (1.25 , 2.2 and $3.5\mu\text{m}$) and the PNe in the survey fields only. The dashed lines represent the three COBE bands and the solid line is the PNe. The COBE distributions have been normalized to give the same area under the histograms as the PNe distribution.

Fig. 15.— Longitude cumulative distribution of the COBE light (1.25, 2.2 and $3.5\mu\text{m}$) in the survey fields only.

Fig. 16.— Longitude cumulative distribution of the COBE light at $2.2\mu\text{m}$ and the PNe in the survey fields only. The solid line is the COBE light cumulative distribution and the *staircase* line represent the PNe cumulative distribution. The ordinate, N , has been normalized to 1.0 for both distributions.

Fig. 17.— Face-on view (XY) and edge-on view (YZ) of Sellwood’s Model. The Sun has been positioned at $(X,Y) = (6,0)$ and is at 30° angle from the major axis of the bar. The edge-on view point is at infinity.

Fig. 18.— Face-on view (XY) and edge-on view (YZ) of Fux’s Model. The Sun has been positioned at $(X,Y) = (8,0)$ and is at 30° angle from the major axis of the bar. The edge-on view point is at infinity.

Fig. 19.— Face-on view (XY) and edge-on view (YZ) of Kalnajs’ Model. The Sun has been positioned at $(X,Y) = (8,0)$ and is at 45° angle from the major axis of the bar. The edge-on view point is at infinity.

Fig. 20.— Face-on view (XY) and edge-on view (YZ) of Zhao’s Model. The Sun has been positioned at $(X,Y) = (8,0)$ and is at 20° angle from the major axis of the bar. The edge-on view point is at infinity.

Fig. 21.— Longitude-velocity diagram for Sellwood’s model with 400 particles. The velocities in this and all following figures are relative to the LSR.

Fig. 22.— Longitude-velocity diagram for Zhao’s model with 1700 particles.

Fig. 23.— Longitude-velocity diagram for Fux’s model with 6000 particles.

Fig. 24.— Longitude-velocity diagram for Kalnajs’ model with 9000 particles.

Fig. 25.— Mean velocity versus longitude (top panel) and mean dispersion versus longitude (lower panel) of the PNe (thin lines), with Kalnajs’ model represented by thick lines.

Fig. 26.— Mean velocity versus longitude (top panel) and mean dispersion versus longitude (lower panel) of the PNe (thin lines), with Fux’s model represented by thick lines.

Fig. 27.— Mean velocity versus longitude (top panel) and mean dispersion versus longitude (lower panel) of the PNe (thin lines), with Sellwood’s model represented by thick lines.

Fig. 28.— Mean velocity versus longitude (top panel) and mean dispersion versus longitude (lower panel) of the PNe (thin lines), with Zhao’s model represented by thick lines.

Fig. 29.— Cumulative distributions over l of the four models and the Survey fields only PNe (heavy line) (all models with $N=400$ and over the same interval in b).

Fig. 30.— Histogram of the distribution of LSR radial velocity for our Survey fields + Catalogue sample in the longitude interval $5^\circ < l < 10^\circ$.

Table 1. $(\langle V \rangle, \sigma)$ versus l for *Survey fields only*

Mean longitude	$\langle V \rangle$	σ	$\langle V \rangle_{error}$	σ_{error}
15°.3	84.9	42.4	12.8	8.6
8°.9	86.8	89.1	26.9	18.2
4°.5	64.4	61.3	18.5	12.5
1°.5	13.9	60.8	18.3	12.4
−0°.9	20.2	103.9	31.3	21.2
−3°.2	−52.4	98.5	29.7	20.1
−6°.1	−54.3	76.8	23.1	15.7
−13°.8	−79.6	90.4	26.1	17.7

Table 2. $(\langle V \rangle, \sigma)$ versus b for *Survey fields only*

Mean latitude	$\langle V \rangle$	σ	$\langle V \rangle_{error}$	σ_{error}
$-5^\circ.7$	7.4	97.7	14.3	9.9
$-8^\circ.1$	11.7	102.5	14.8	10.4

Table 3. $(\langle V \rangle, \sigma)$ versus l for *Survey fields + Catalogue*

Mean longitude	$\langle V \rangle$	σ	$\langle V \rangle_{error}$	σ_{error}
24°.1	138.2	56.1	10.2	7.1
14°.2	74.8	54.3	9.9	6.9
9°.2	76.5	84.1	15.4	10.7
5°.9	56.8	81.3	14.8	10.3
3°.5	46.8	96.2	17.6	12.2
1°.2	-20.8	74.9	13.7	9.5
-0°.7	17.3	103.5	18.9	13.1
-2°.5	-16.5	107.1	19.6	13.6
-4°.4	-66.9	80.6	14.7	10.2
-8°.9	-68.9	79.0	14.4	10.0
-15°.8	-93.9	62.4	11.4	7.9
-24°.5	-135.1	65.4	11.8	8.2

Table 4. ($\langle V \rangle, \sigma$) versus b for *Survey fields + Catalogue*

Mean latitude	$\langle V \rangle$	σ	$\langle V \rangle_{error}$	σ_{error}
8°.2	-13.9	96.7	12.3	8.6
4°.2	-6.7	118.0	15.1	10.6
-3°.8	-6.3	124.9	16.0	11.2
-5°.0	17.9	100.9	12.9	9.1
-6°.6	-4.6	103.7	13.3	9.3
-9°.7	15.7	122.5	15.7	11.0

Table 5. Comparison Studies

Study	region (l, b)	symbol
Minniti (1996a) ^a	$(8^\circ, 7^\circ)$	\triangle
	$(12^\circ, 3^\circ)$	\circ
	$(10^\circ, -7.6^\circ)$	\star
Harding and Morrison (1993) ^a	$(-10^\circ, -10^\circ)$	\diamond
Terndrup et al. (1995) BW	$(1^\circ, -3.9^\circ)$	\blacksquare
Ibata & Gilmore (1995b)	$(-25^\circ, -12^\circ)$	$*$
	$(-15^\circ, -12^\circ)$	
	$(-5^\circ, -12^\circ)$	

^a filled = metal-rich and open = metal-poor

Table 6. Kolmogorov-Smirnov test results

λ (μm)	D	Probability
1.25	0.1053	0.2319
2.2	0.0991	0.2963
3.5	0.1024	0.2612

Table 7. Suggested parameters for each model.

Model	Total # of particles	R_{\circ} model units	ϕ degrees	V_{scale} (km-s $^{-1}$) per model units	$V_{\circ T}$ (km-s $^{-1}$)
Sellwood	43802	6	30	300.0	–
Zhao	32634	8	20	291.0	220.0
Fux	200000	8	30	927.5	213.0
Kalnajs	248000	8	45	150.0	215.0

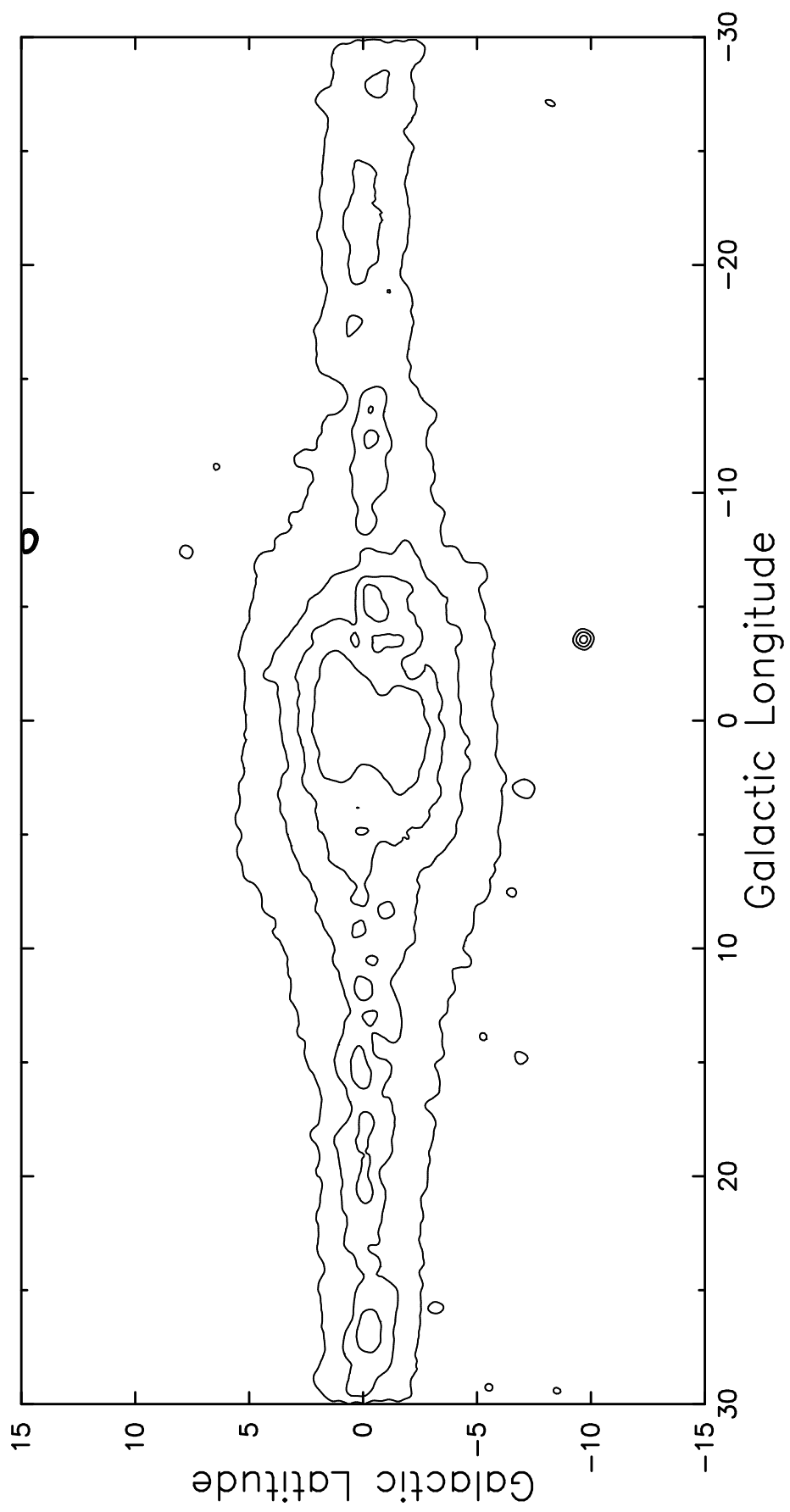
Table 8. Search for the best parameters in models.

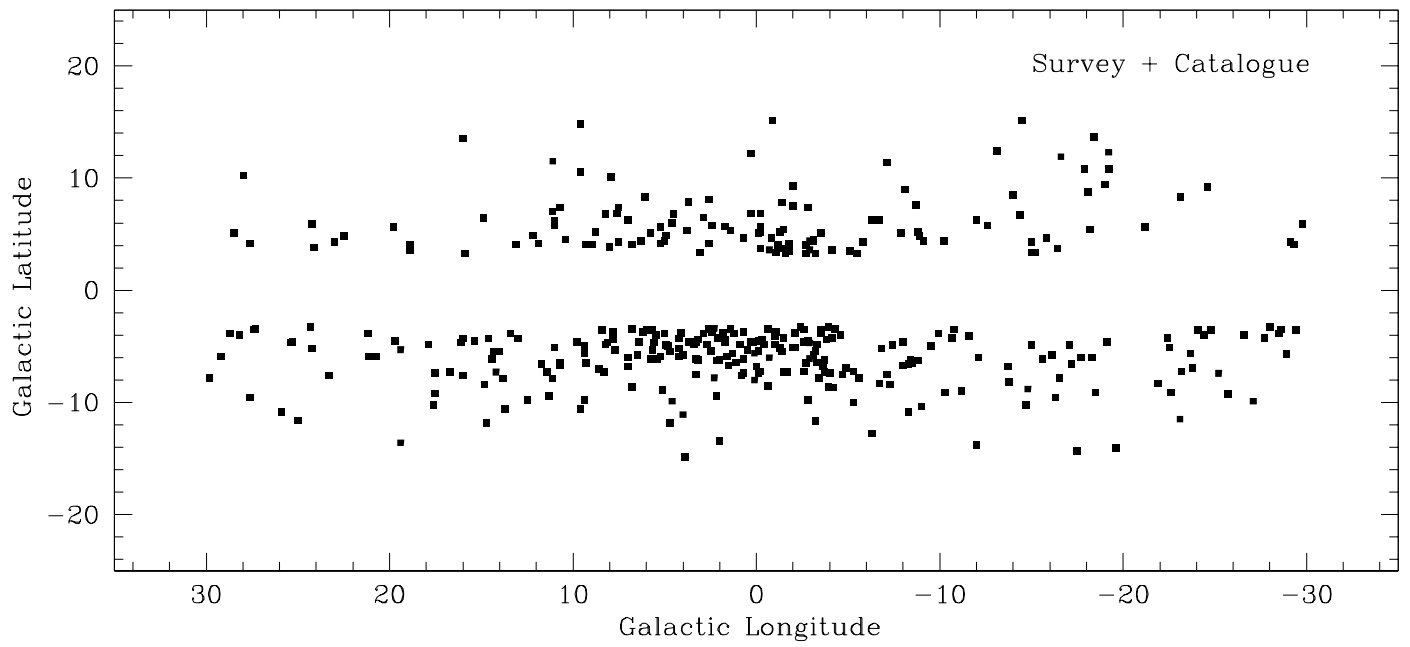
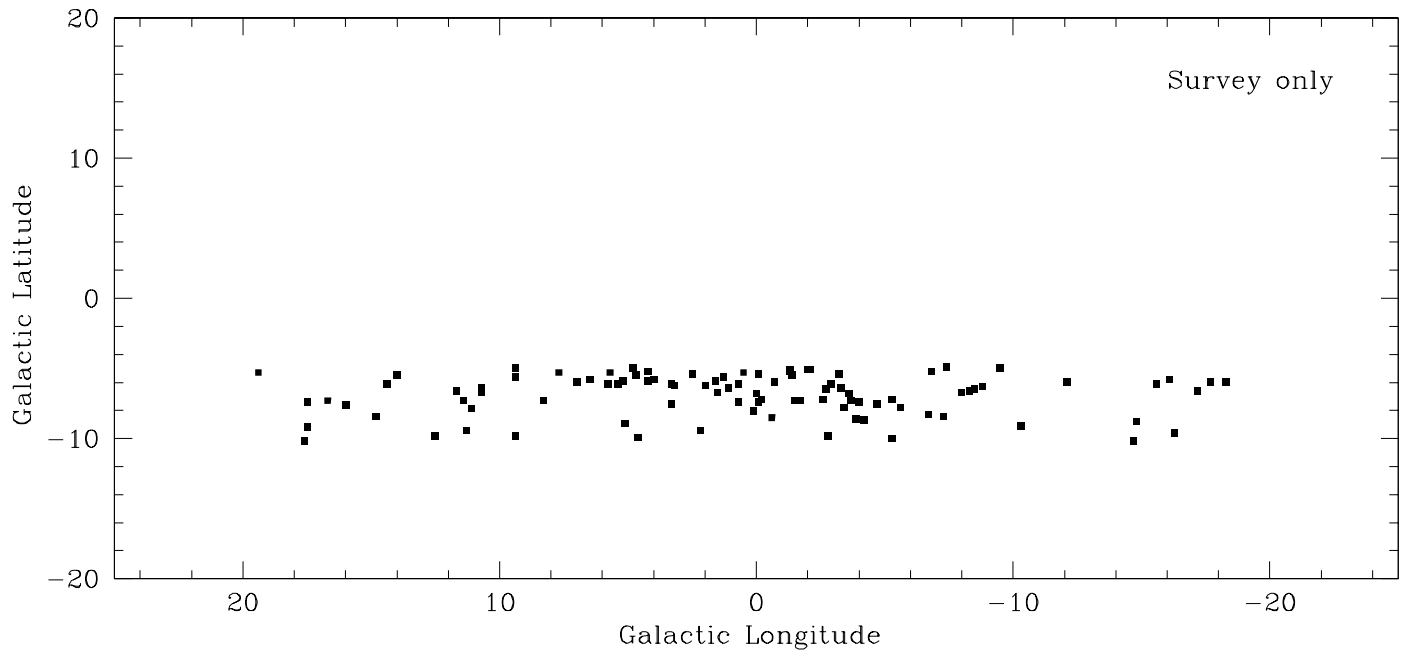
Model	# of fitted particles	Parameters	Median
Sellwood	400	R_{\circ}	$7.3^{+0.6}_{-0.2}$
		ϕ	13^{+26}_{-12}
		V_{scale}	297^{+78}_{-54}
		$V_{\circ T}$	211^{+17}_{-9}
Zhao	1700	R_{\circ}	$7.2^{+0.8}_{-0.2}$
		ϕ	27^{+44}_{-9}
		V_{scale}	218^{+41}_{-23}
		$V_{\circ T}$	212^{+17}_{-11}
Fux	6000	R_{\circ}	$8.6^{+0.3}_{-0.5}$
		ϕ	9^{+17}_{-6}
		V_{scale}	751^{+93}_{-93}
		$V_{\circ T}$	212^{+15}_{-10}
Kalnajs	9000	R_{\circ}	$8.1^{+0.8}_{-0.6}$
		ϕ	53^{+26}_{-43}
		V_{scale}	170^{+23}_{-18}
		$V_{\circ T}$	217^{+18}_{-13}

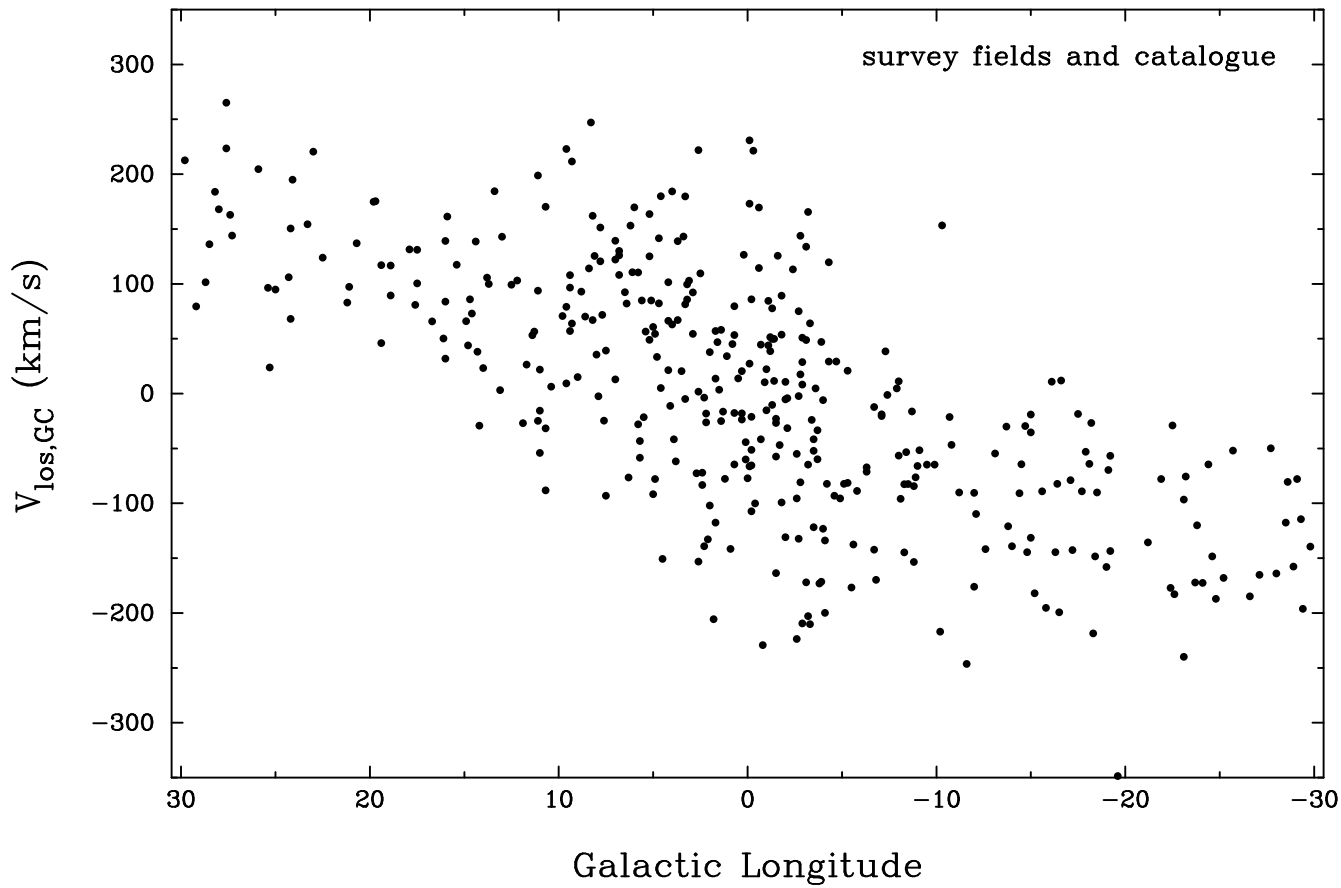
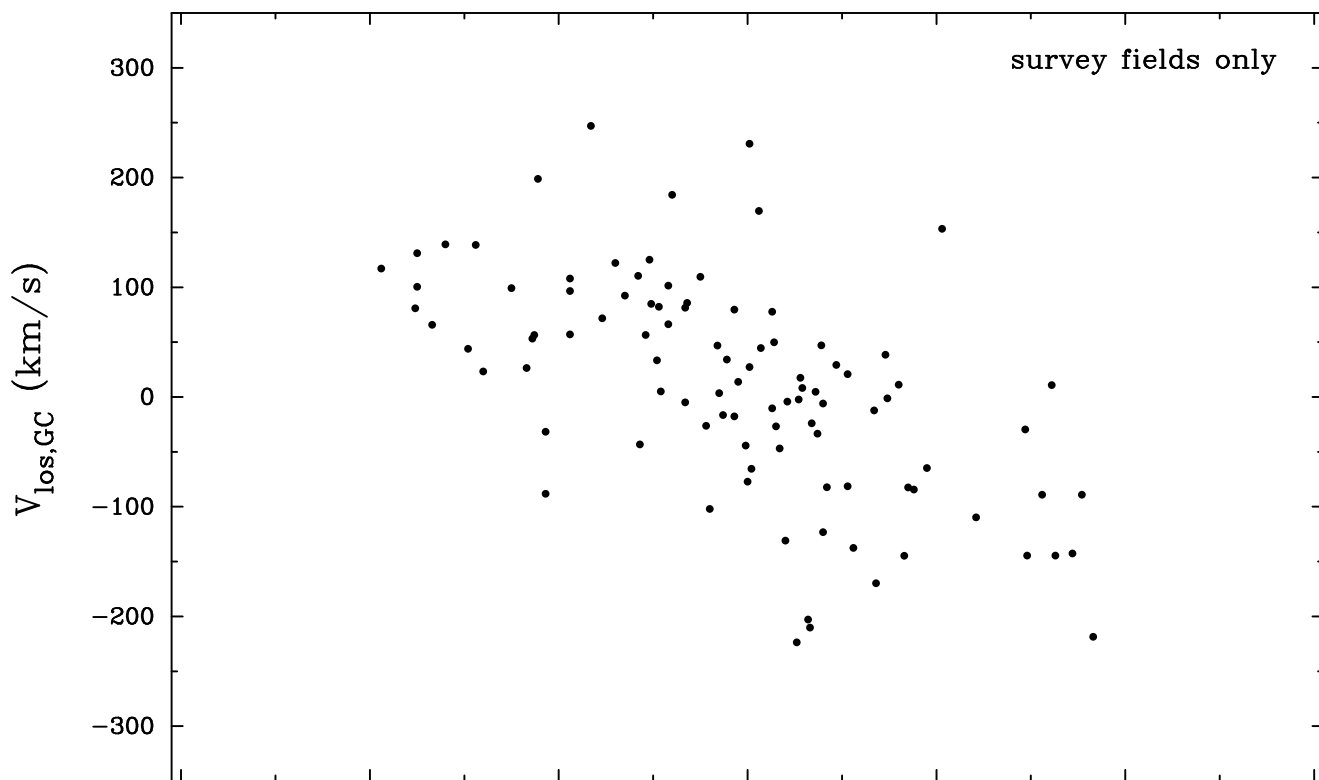
Note. — R_{\circ} is in model units, ϕ is in degrees, V_{scale} is in km s^{-1} per model units and $V_{\circ T}$ is in km s^{-1}

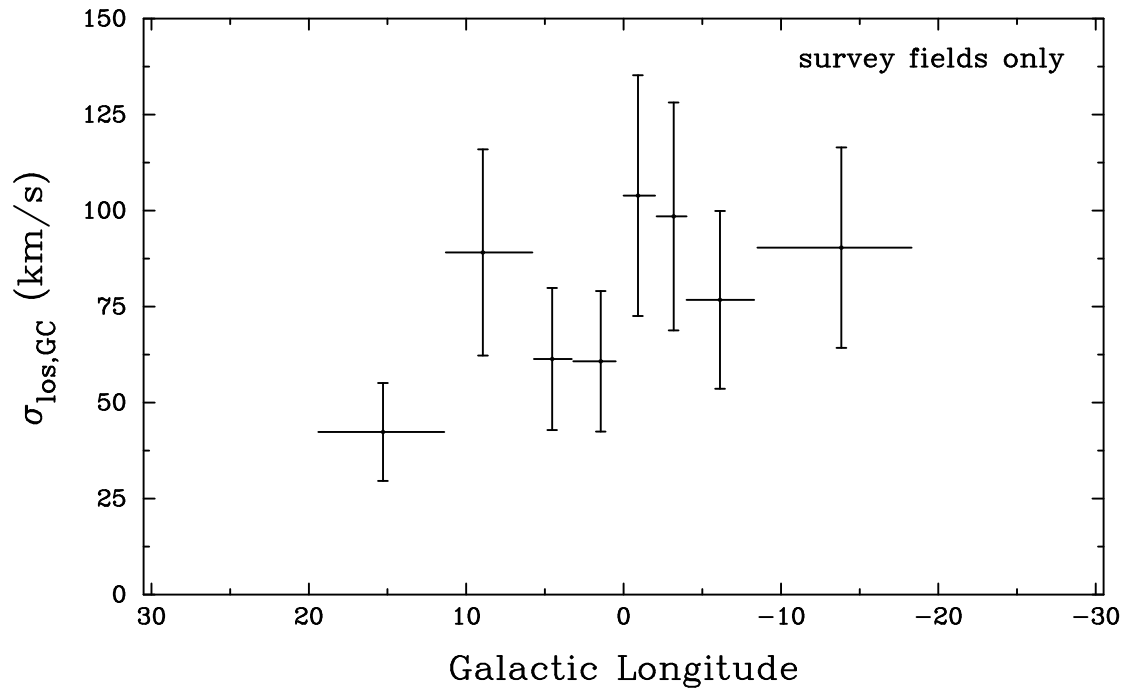
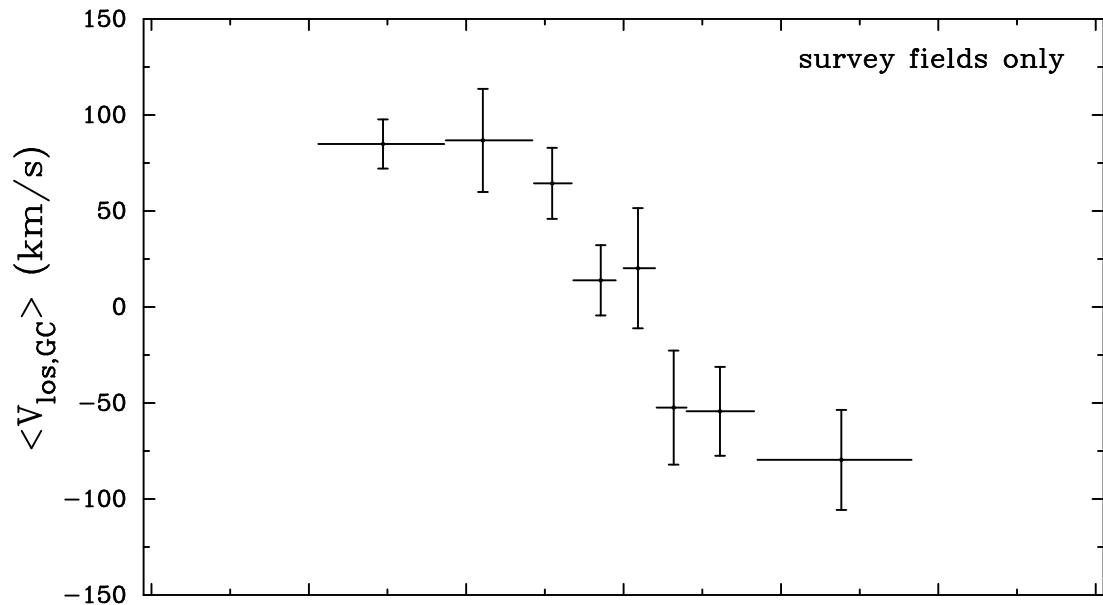
Table 9. $\ln W$ comparison for each sets of models.

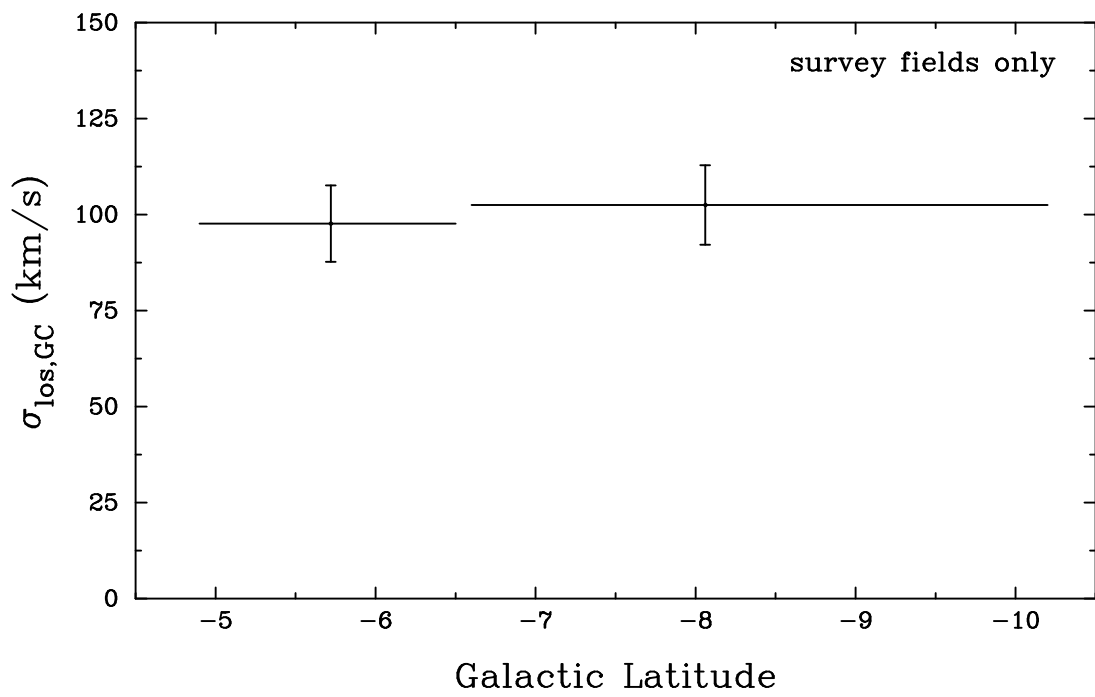
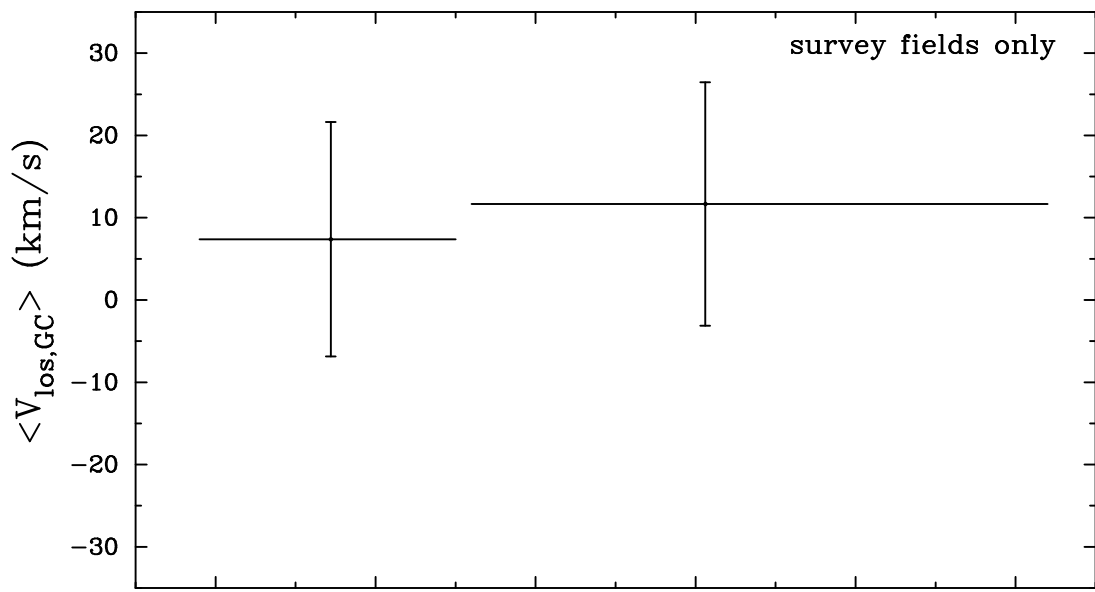
Model	$\ln W$		
	400	1700	6000
Sellwood	129.6
Zhao	128.45	239.25	...
Fux	126.67	237.47	352.75
Kalnajs	126.16	237.95	350.82
$\sigma(\text{sampling})$	1.84	1.89	1.50

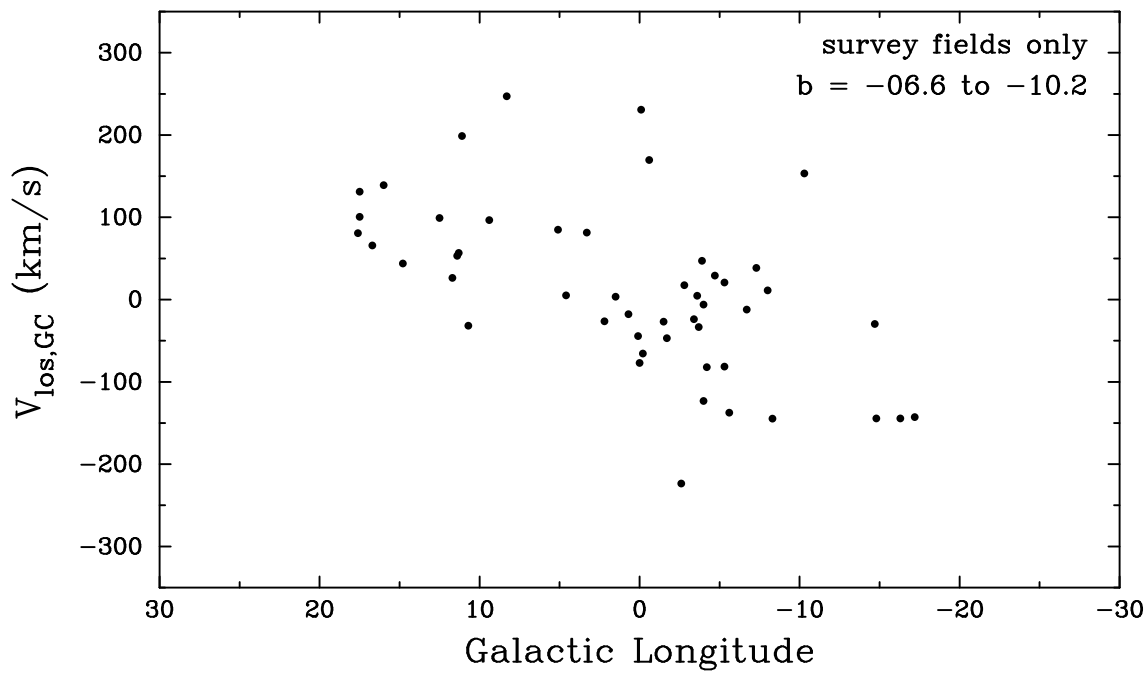
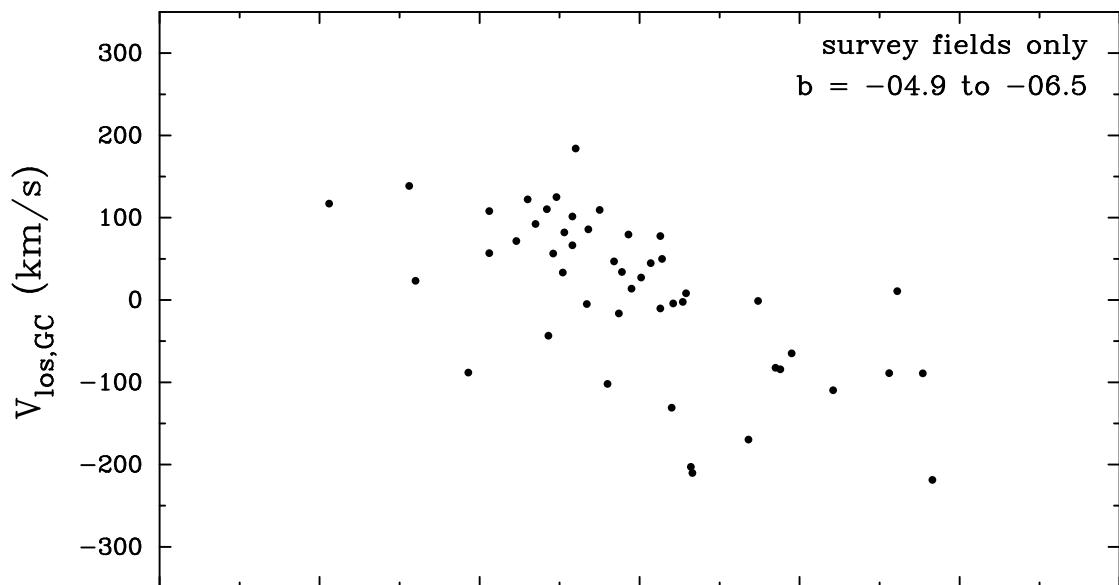


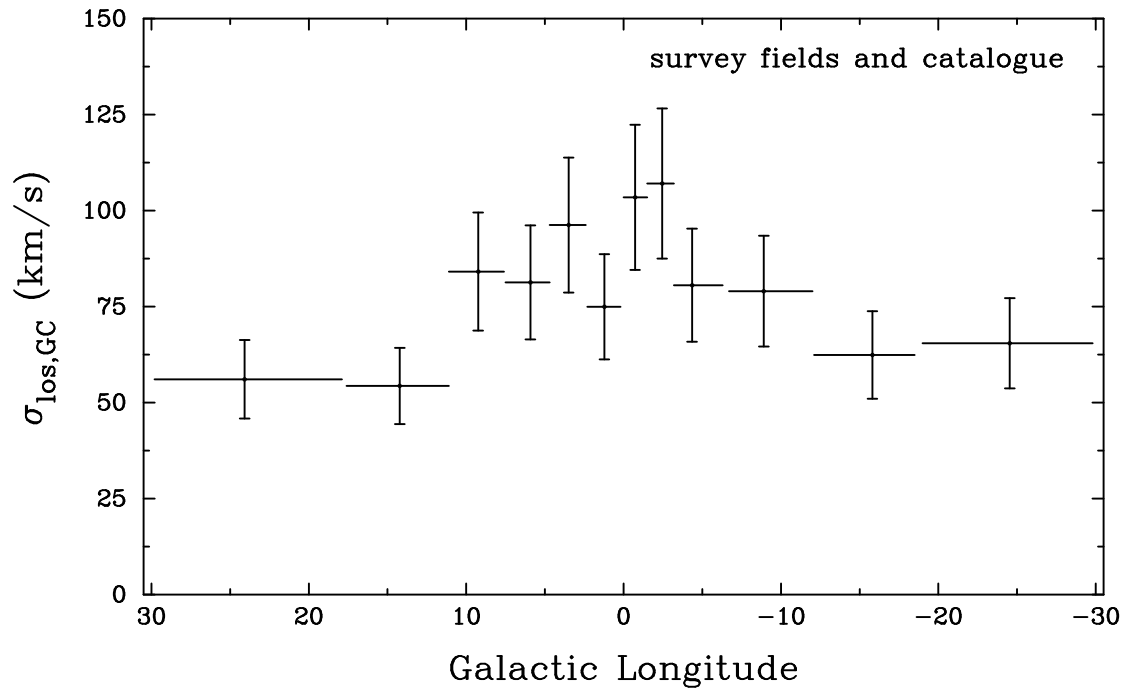
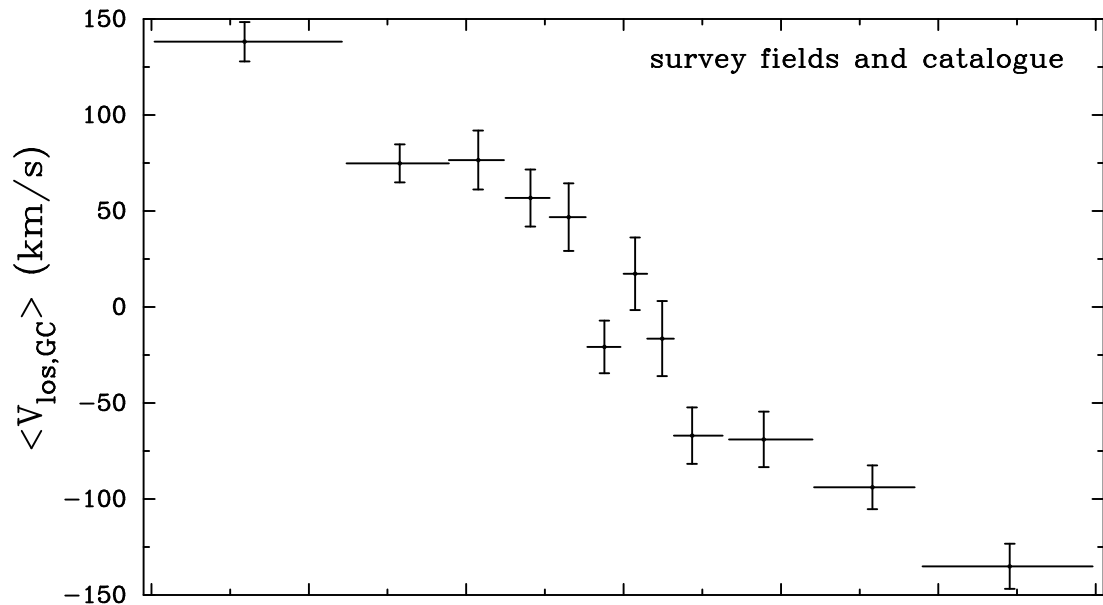


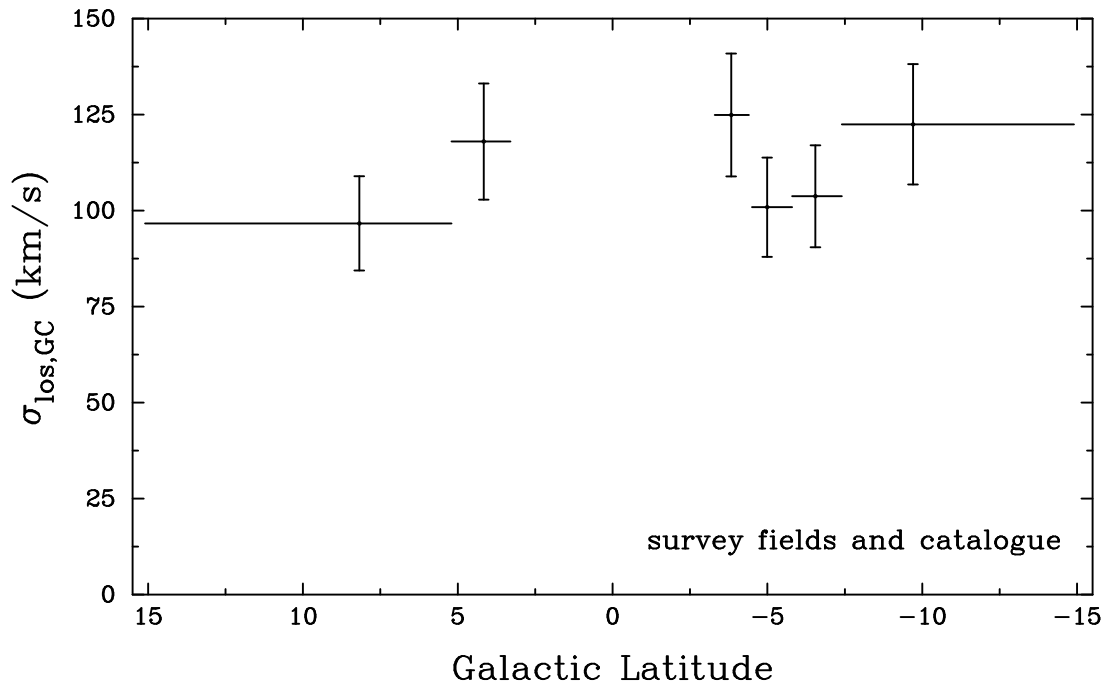
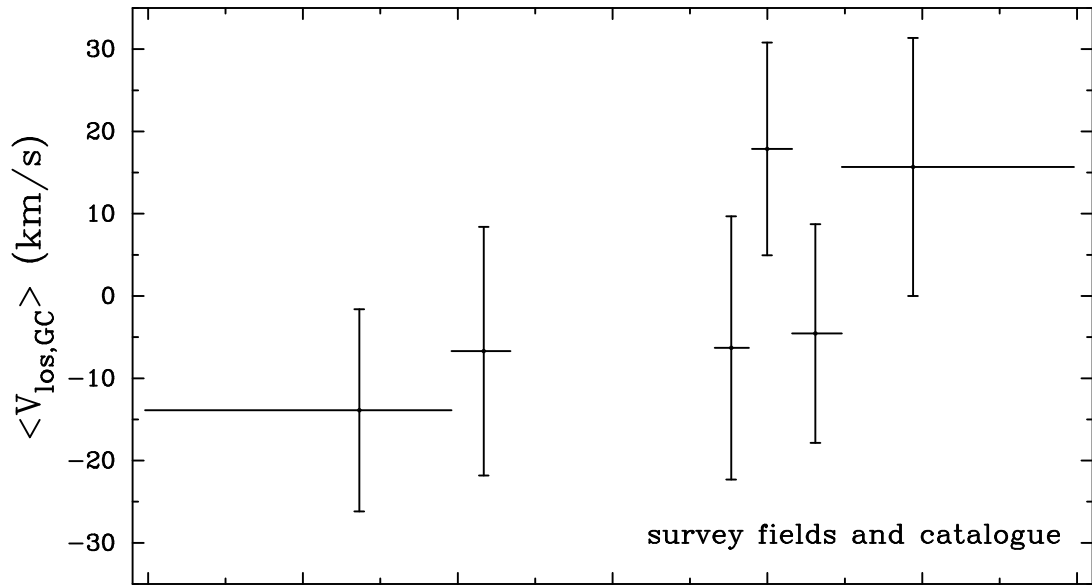


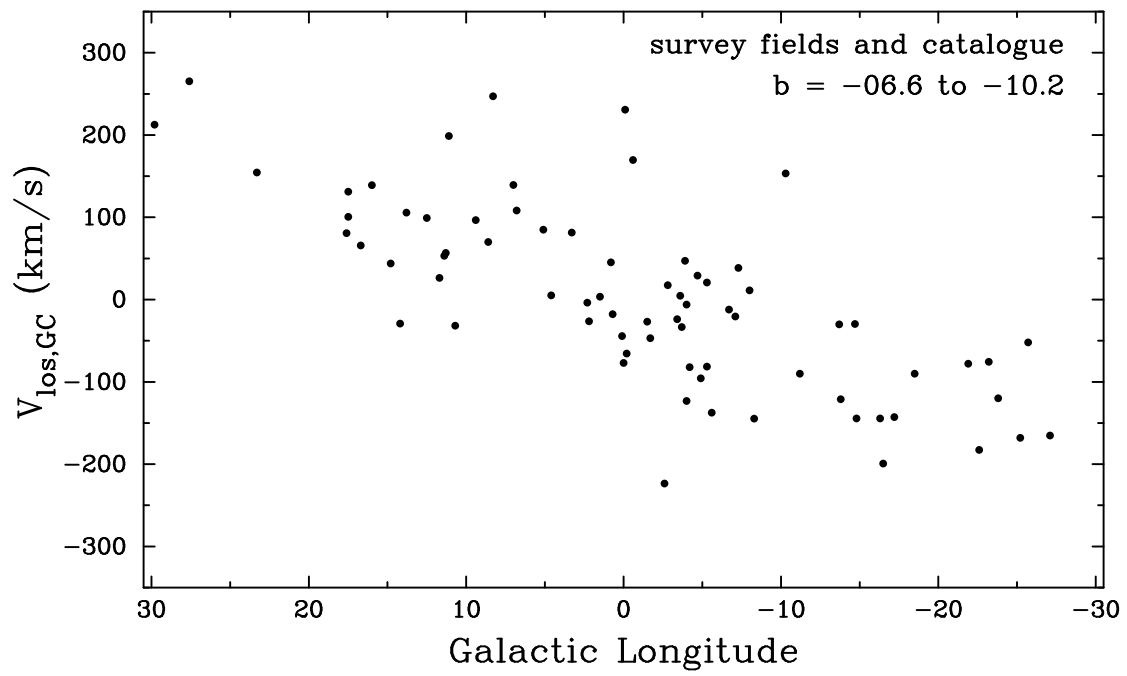
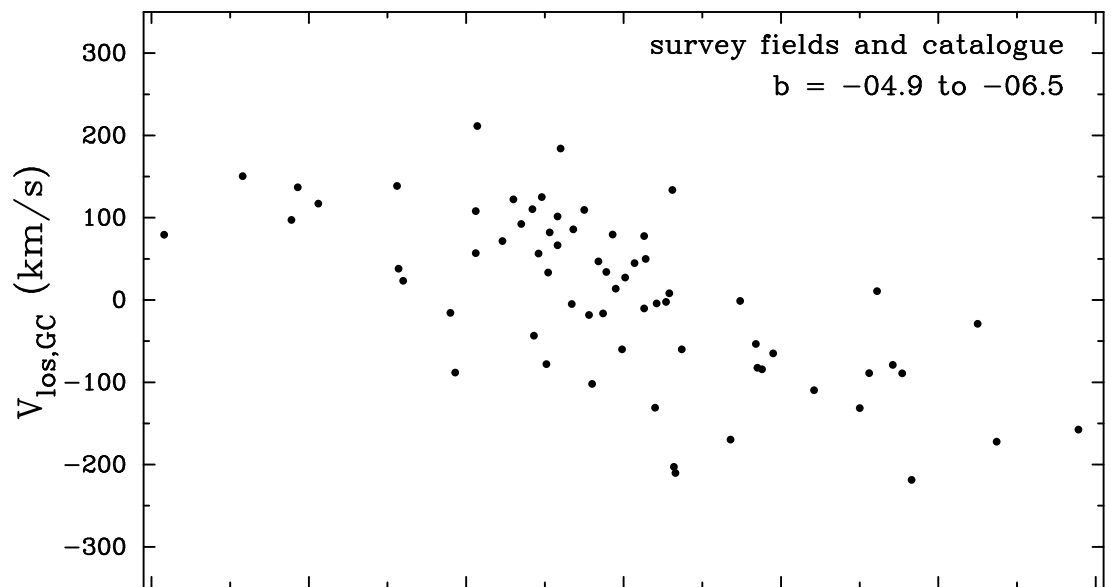


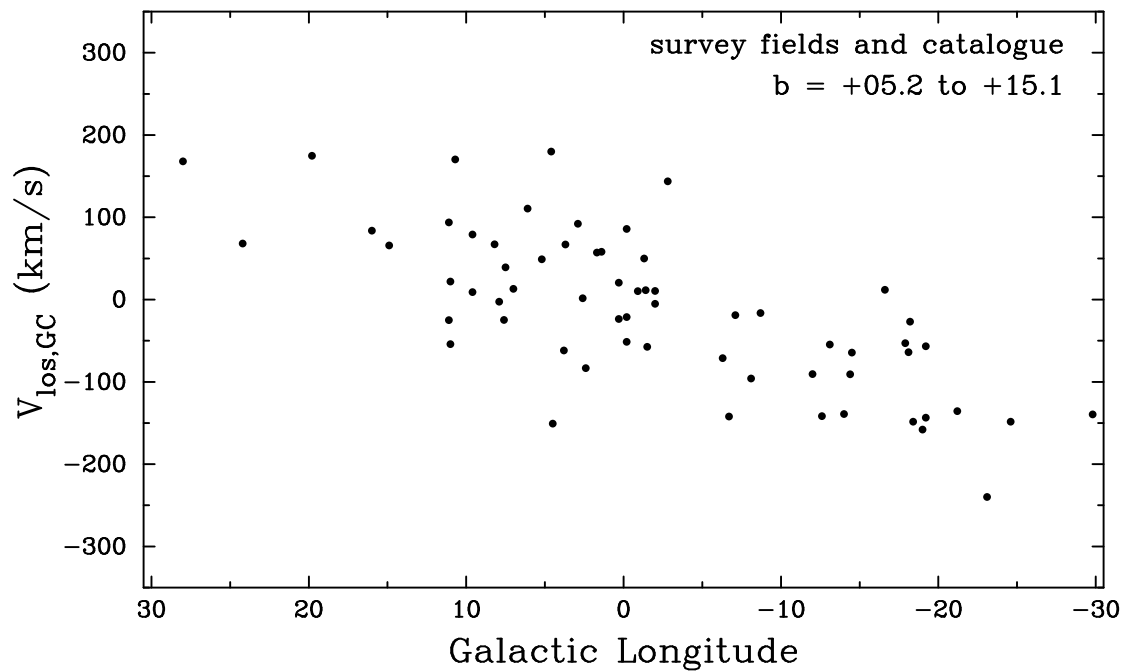
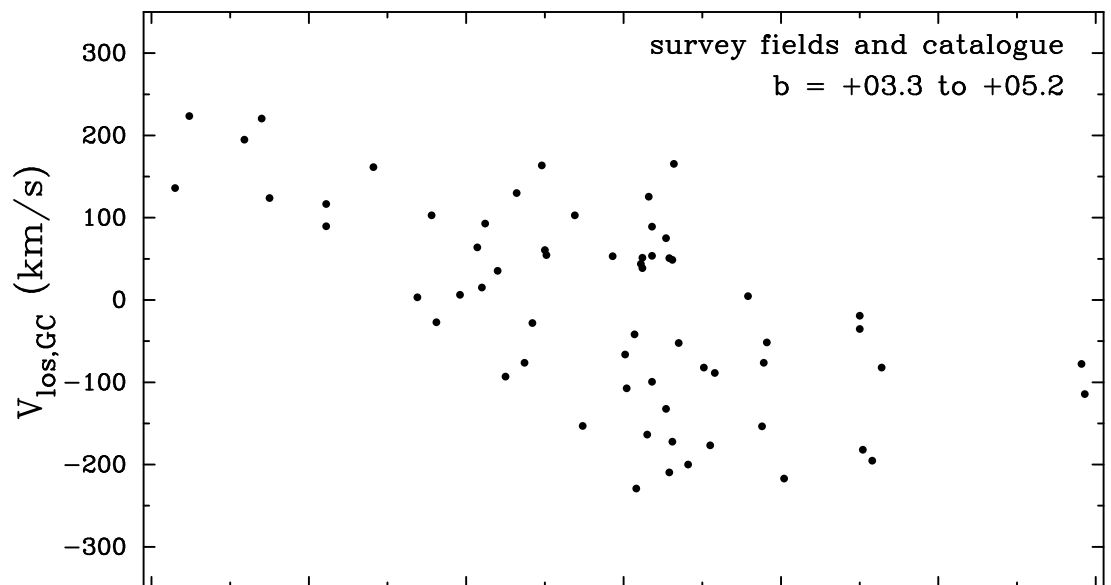


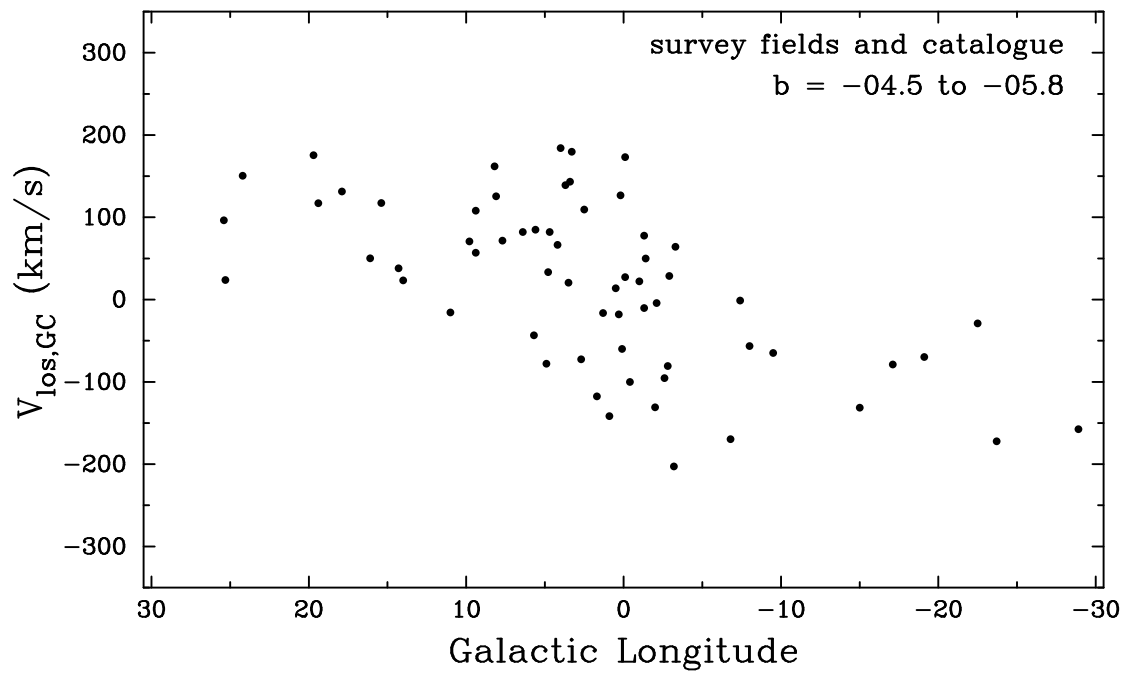
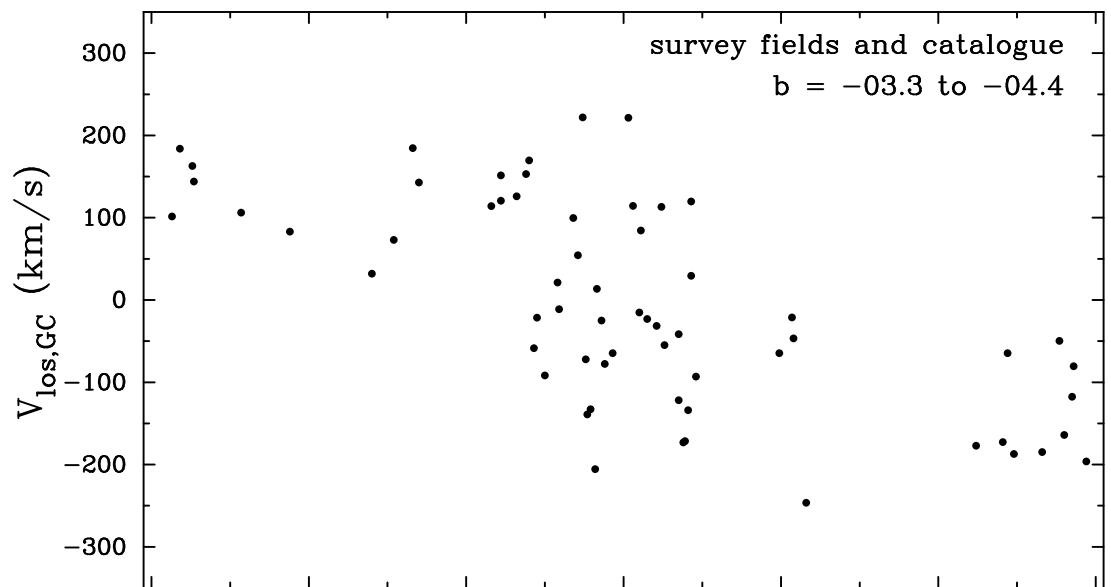


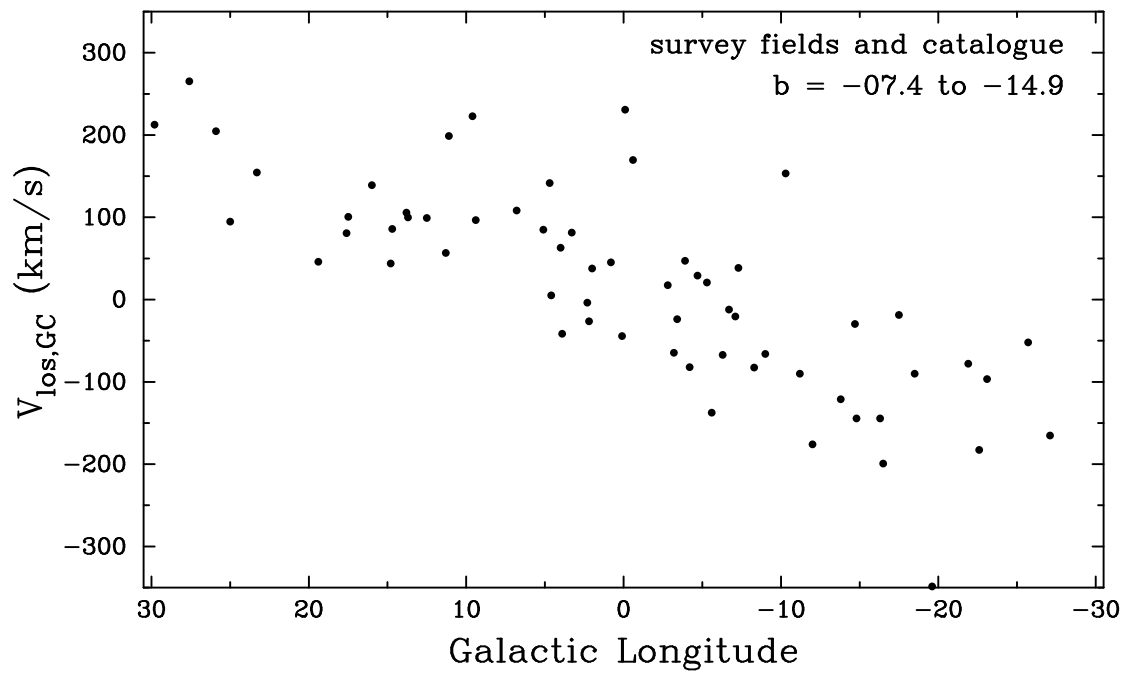
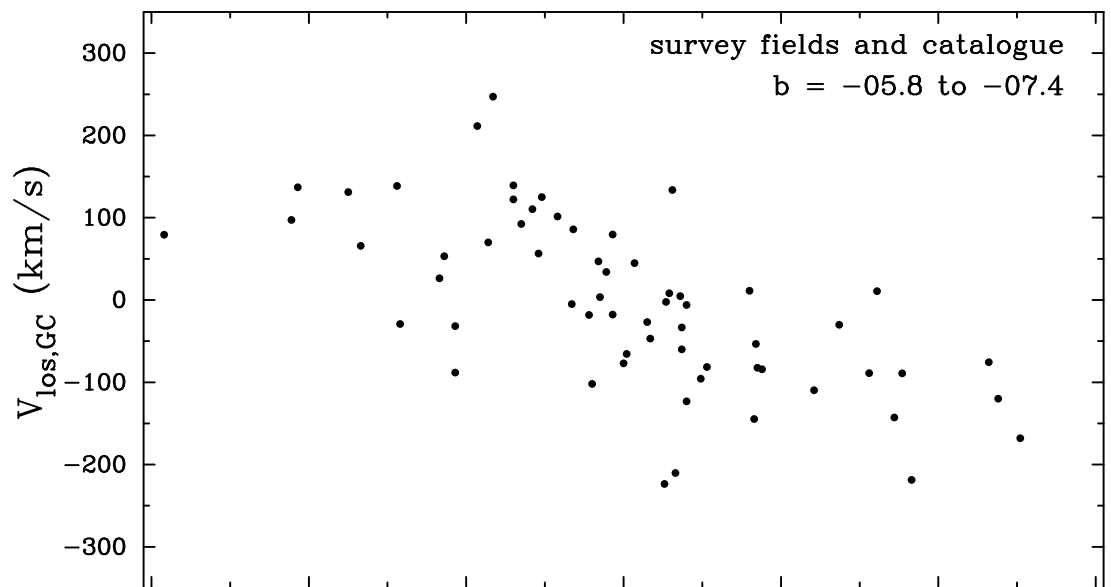


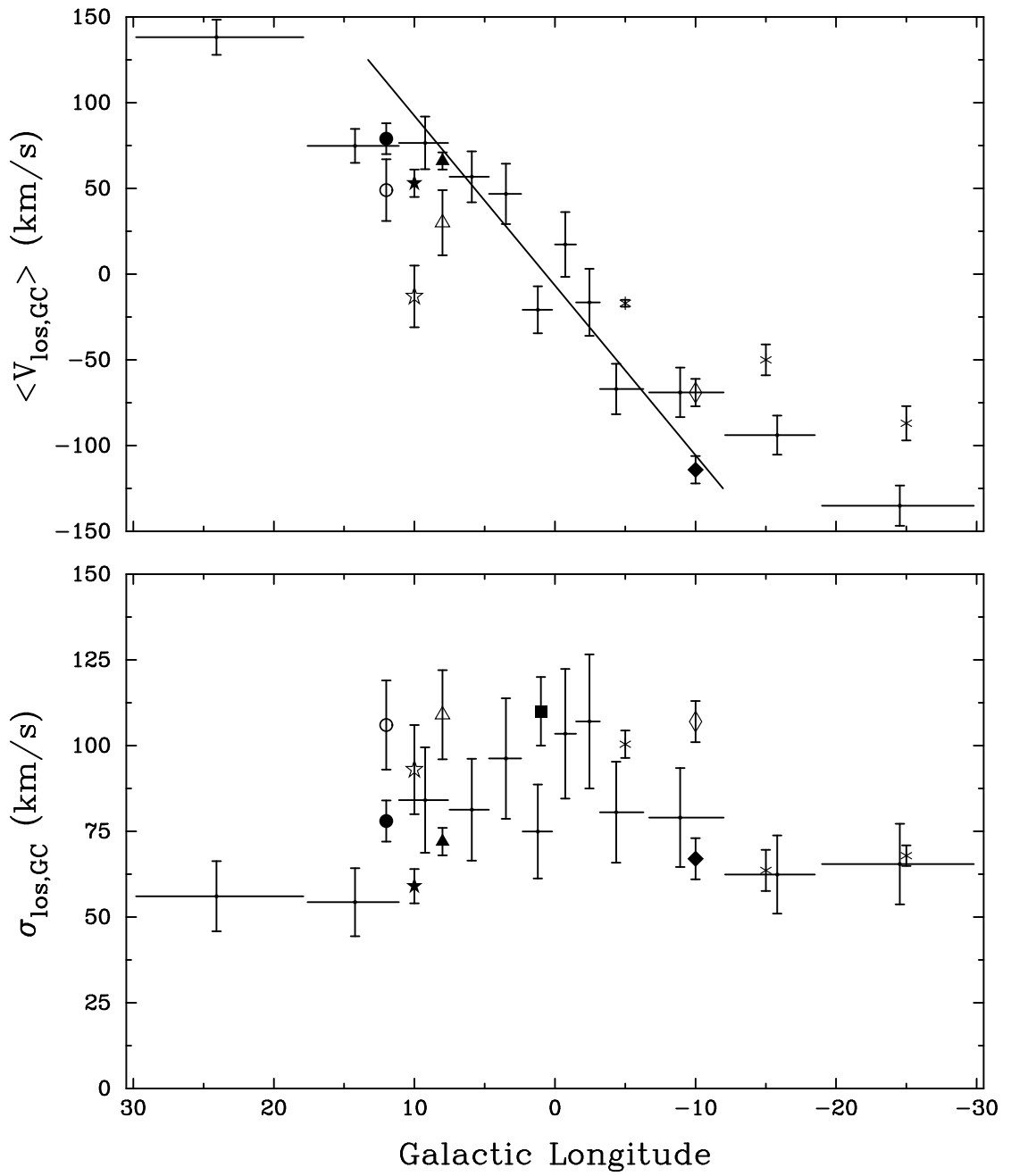


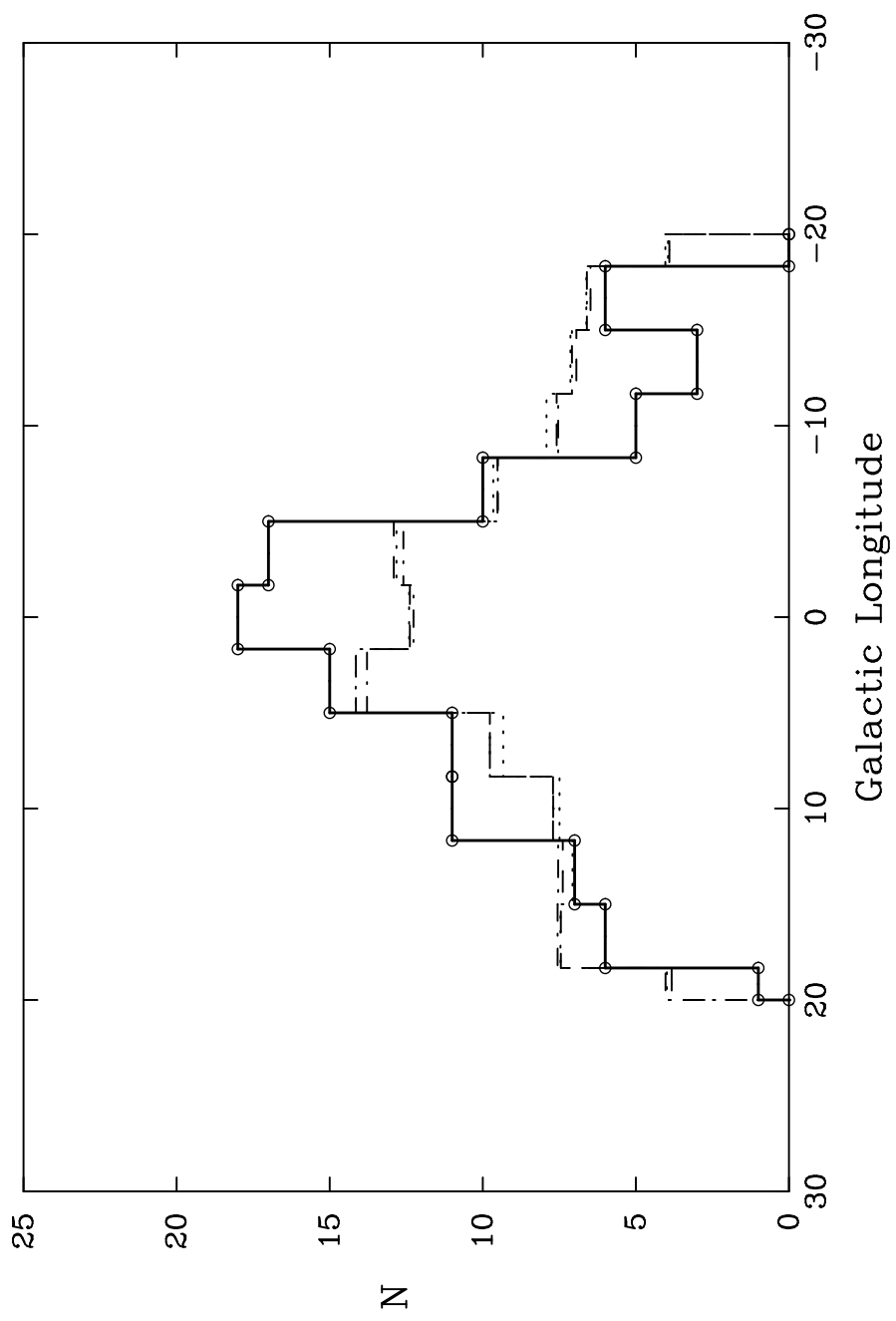


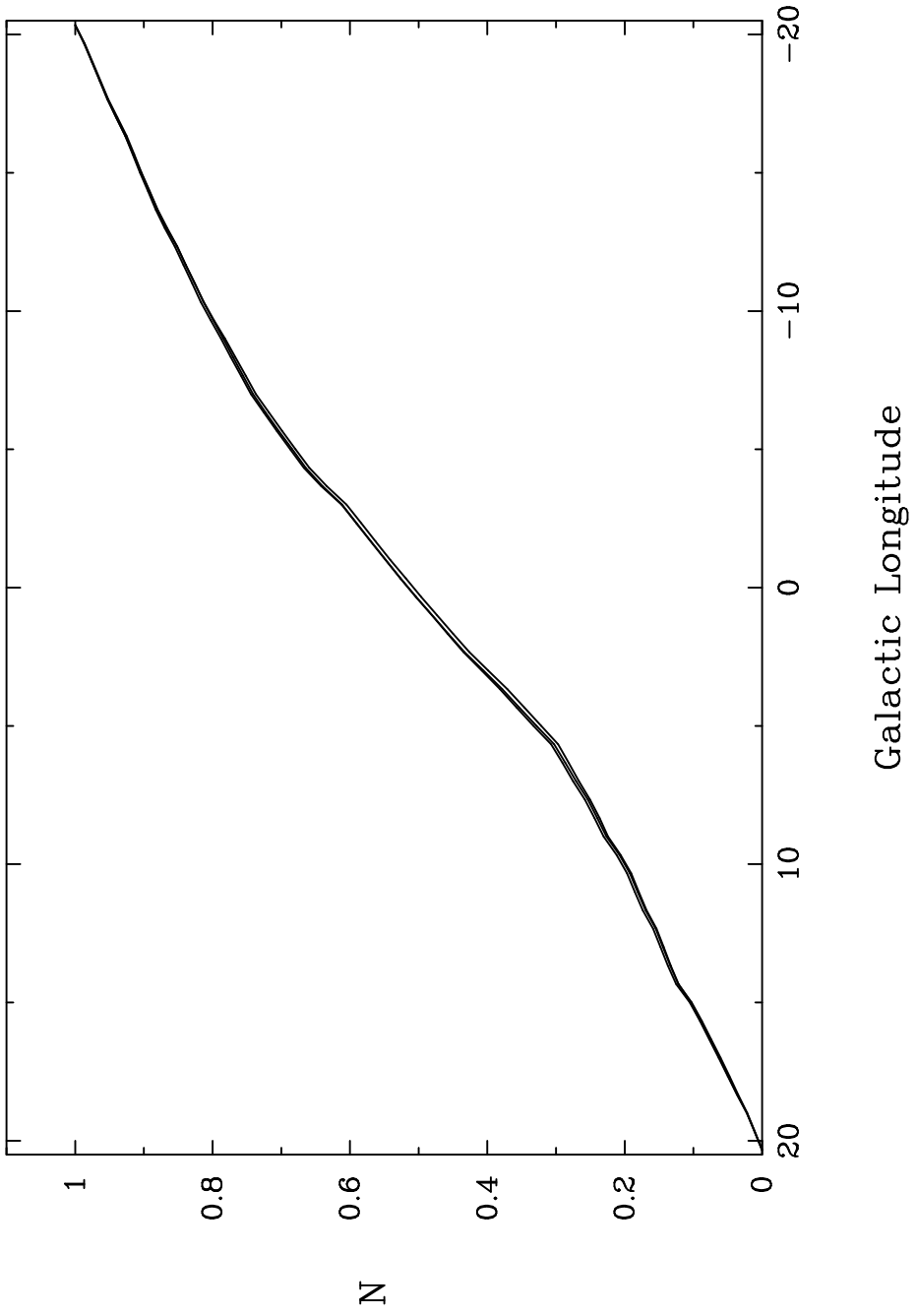


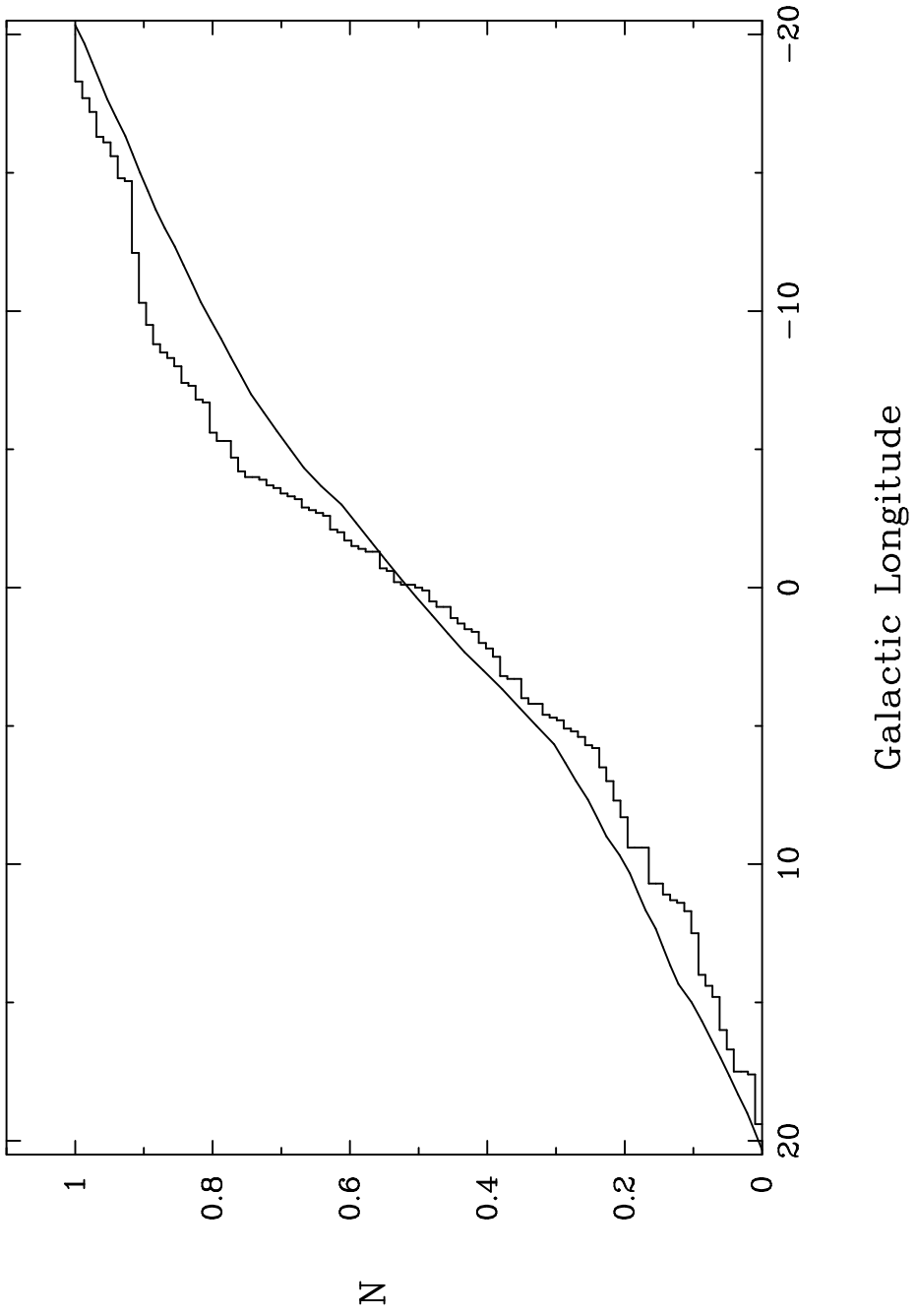


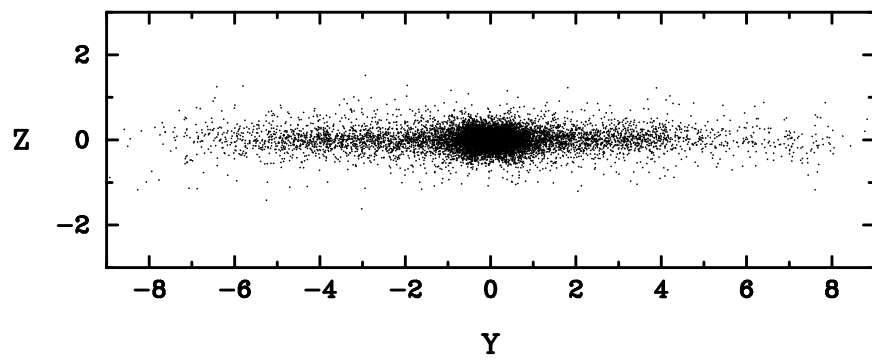
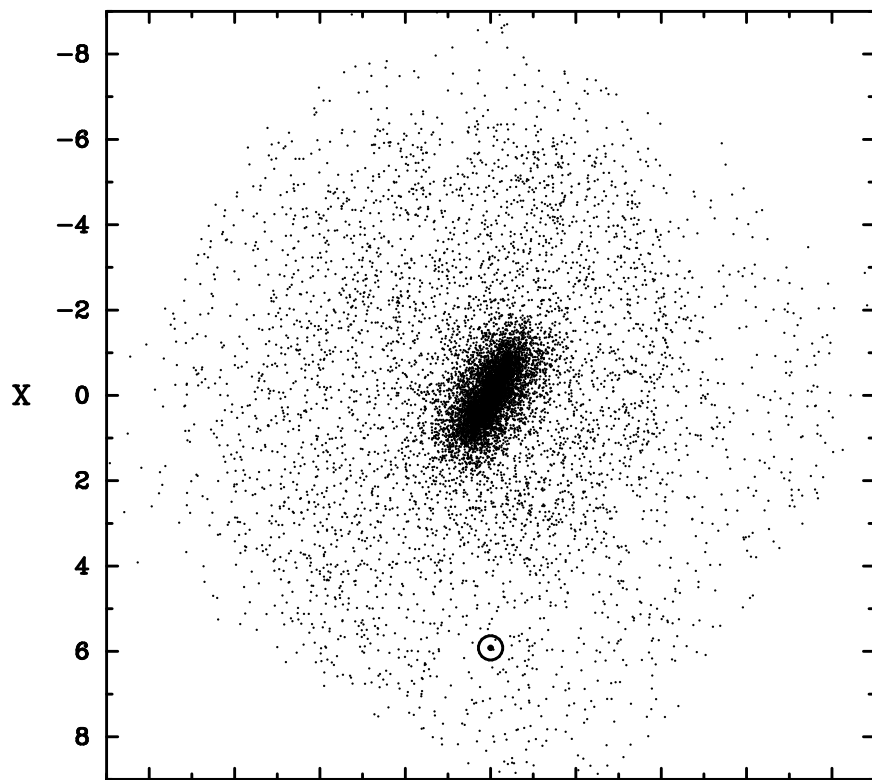












This figure "BeaulieuSF.f18.jpg" is available in "jpg" format from:

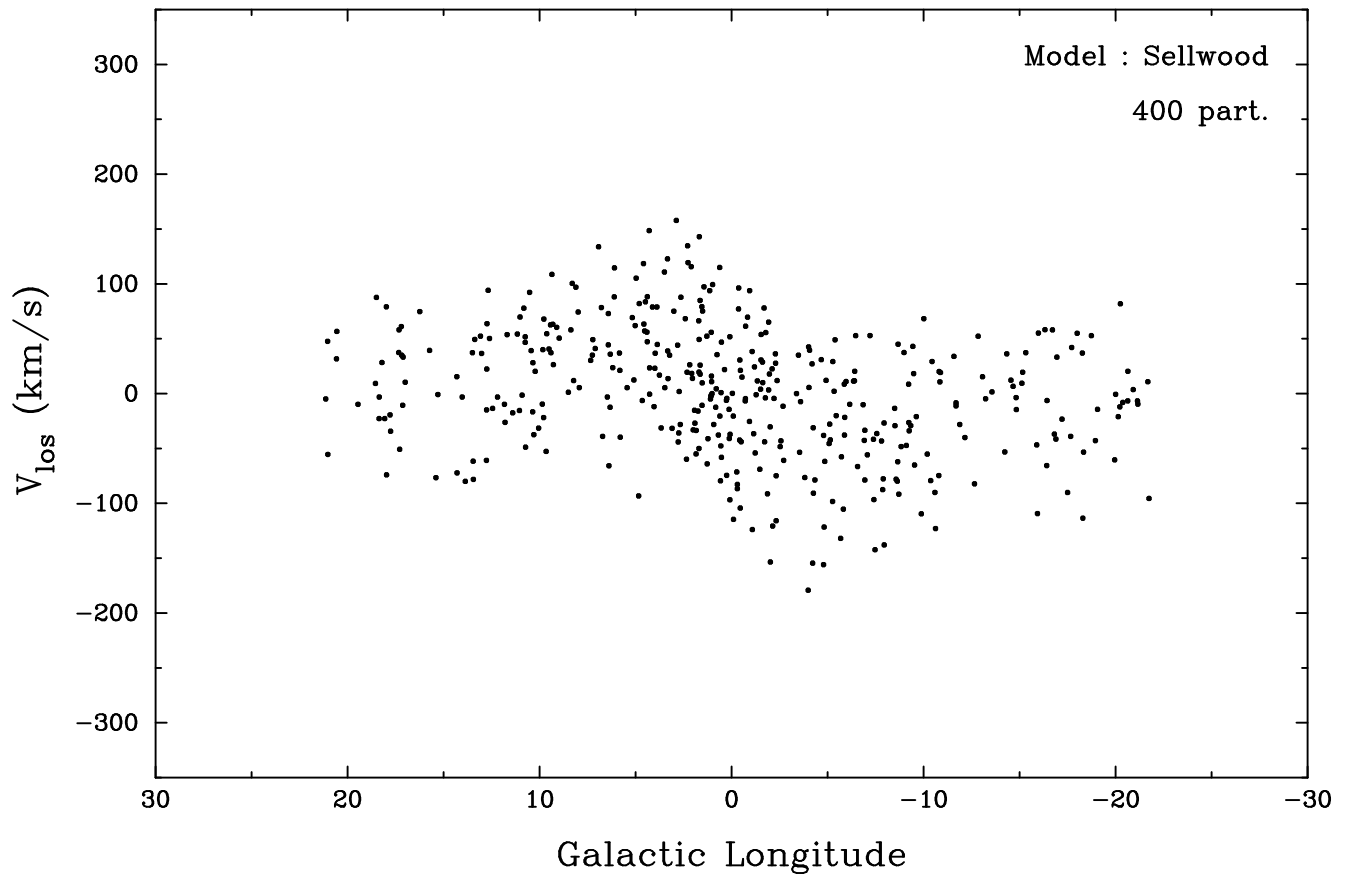
<http://arxiv.org/ps/astro-ph/0005086v1>

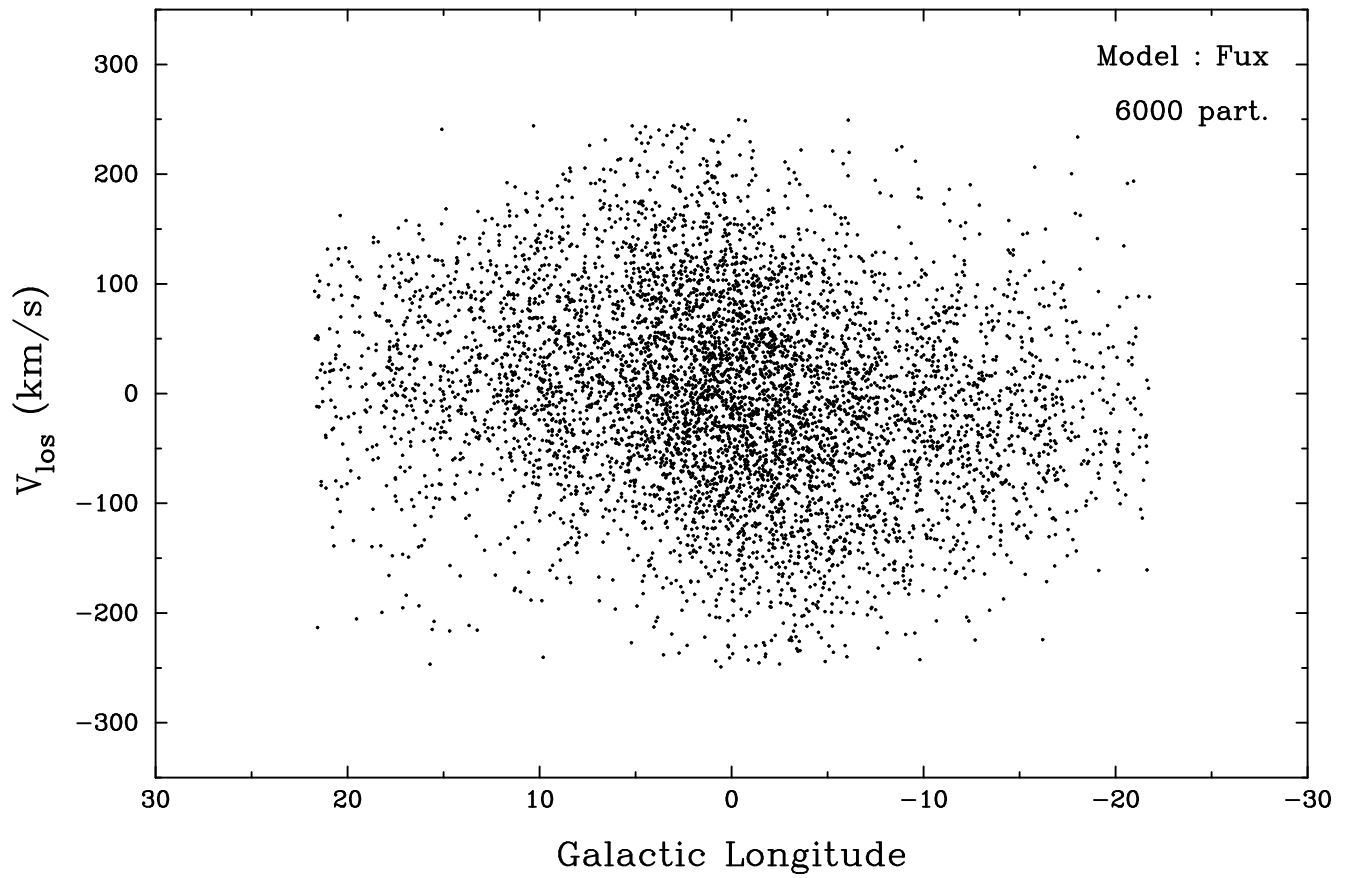
This figure "BeaulieuSF.f19.jpg" is available in "jpg" format from:

<http://arxiv.org/ps/astro-ph/0005086v1>

This figure "BeaulieuSF.f20.jpg" is available in "jpg" format from:

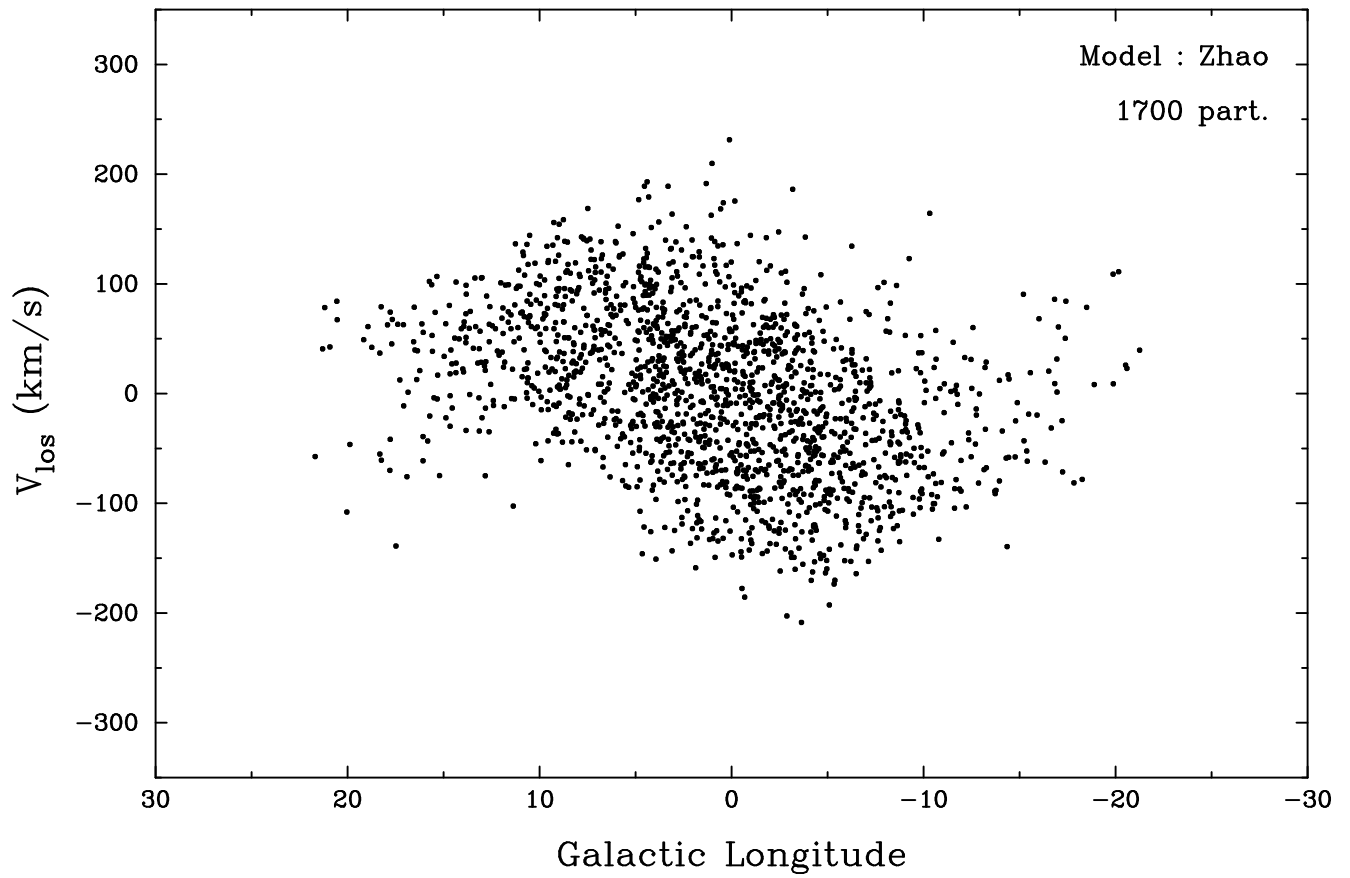
<http://arxiv.org/ps/astro-ph/0005086v1>

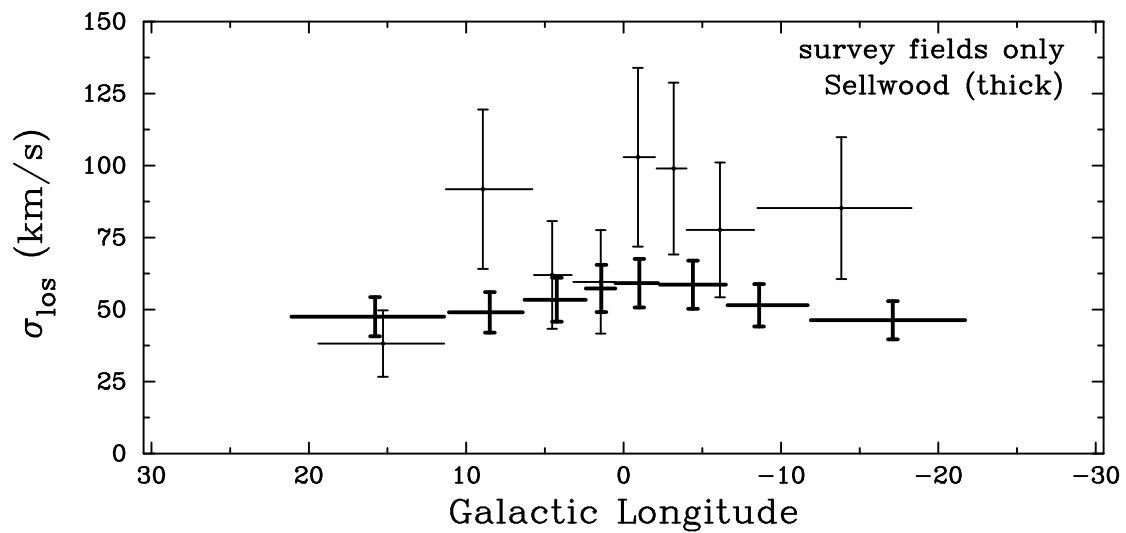
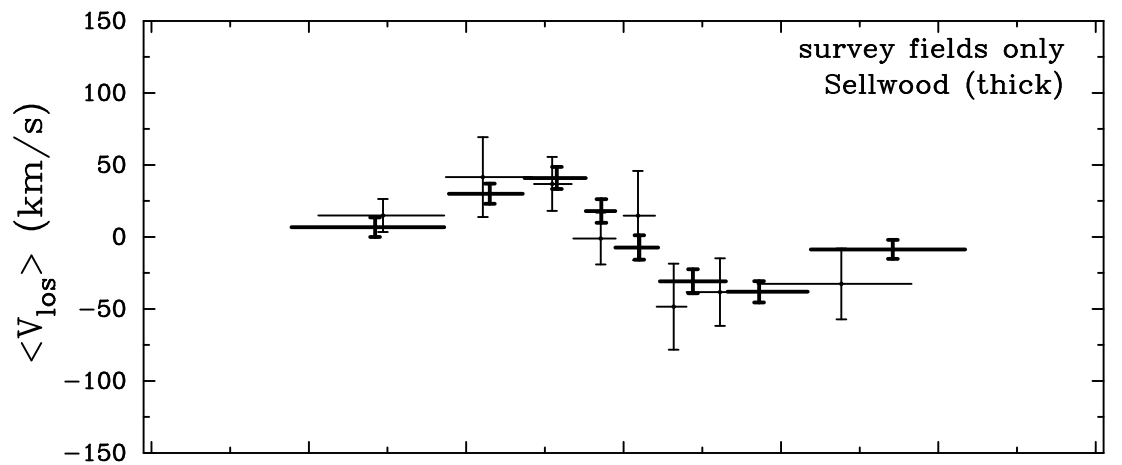


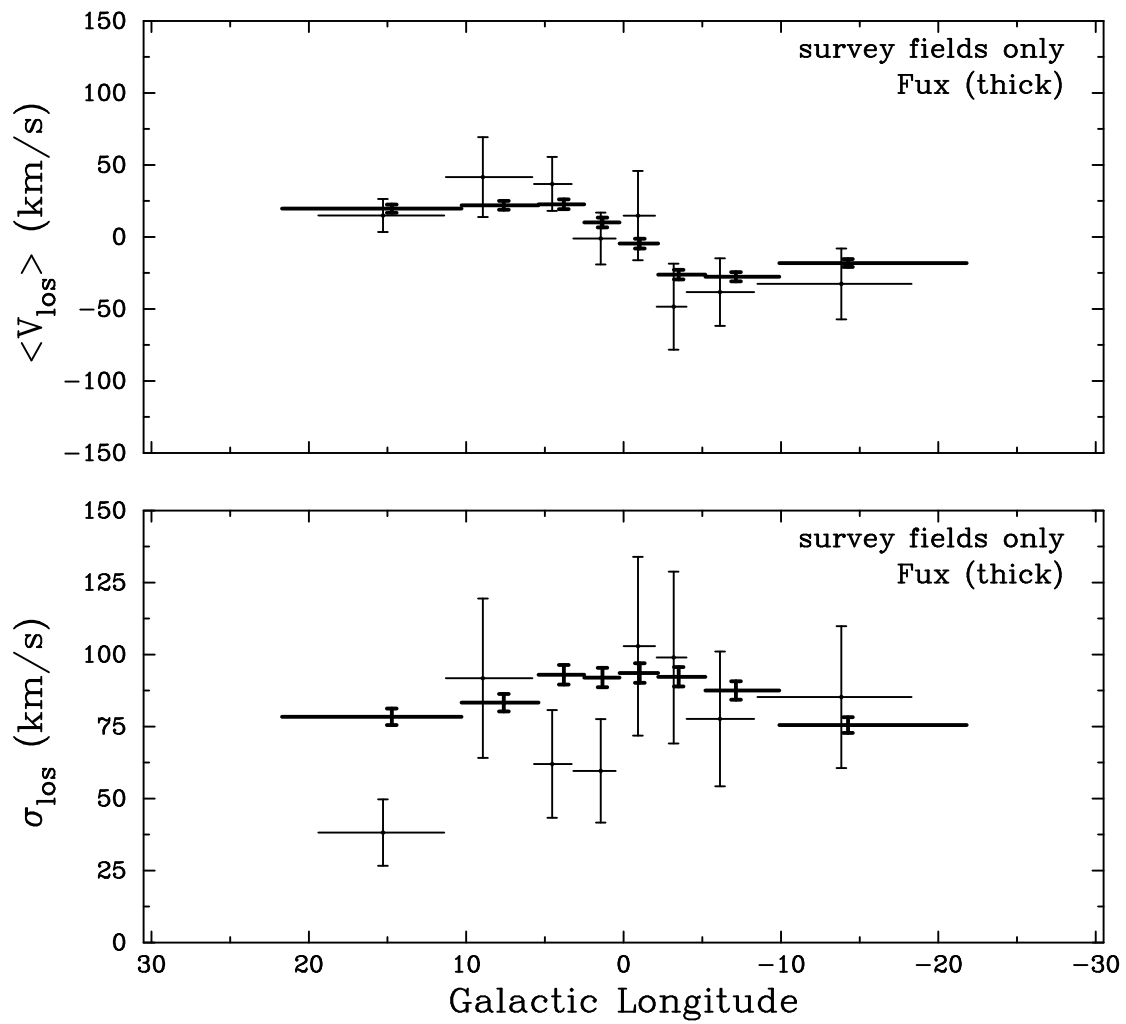


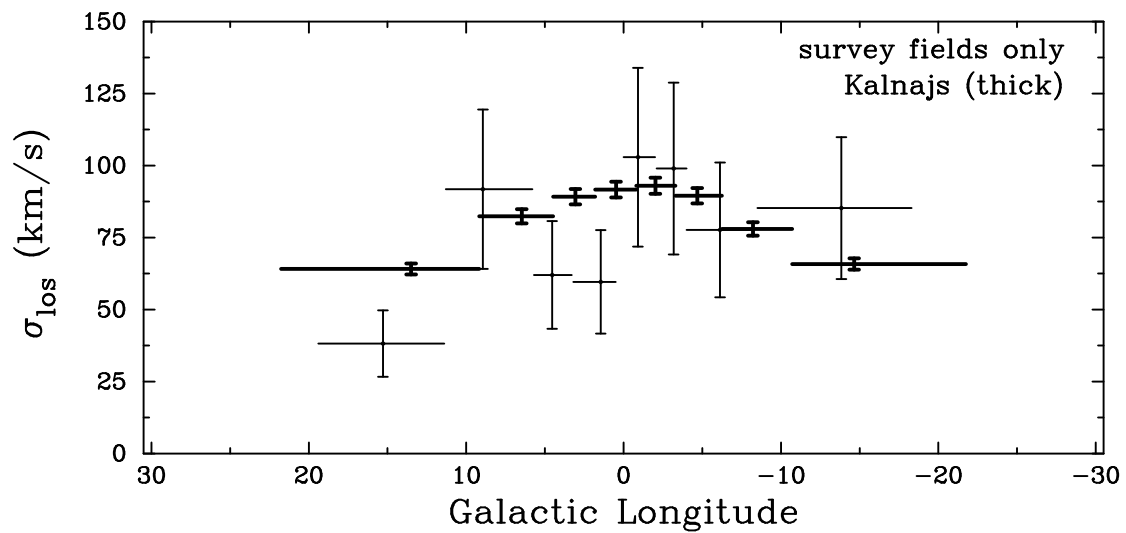
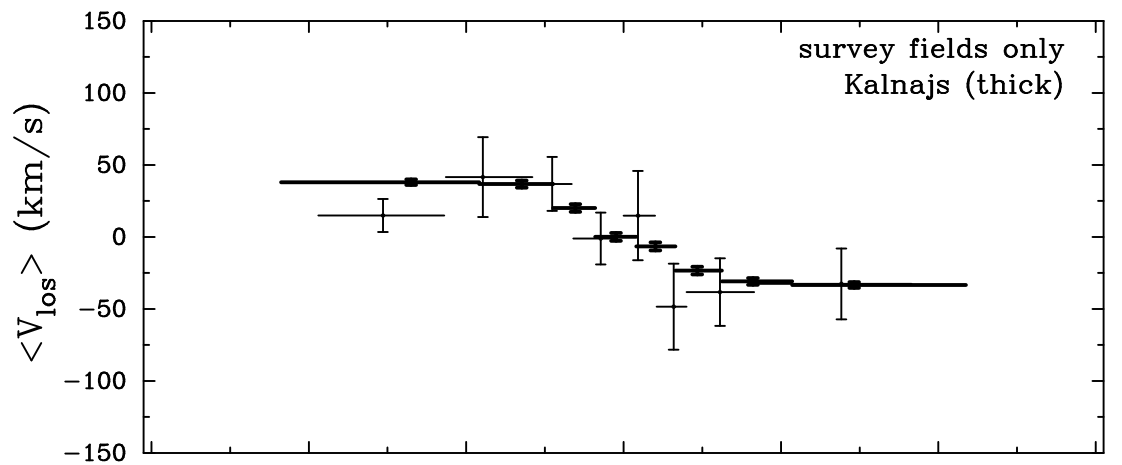
This figure "BeaulieuSF.f23.jpg" is available in "jpg" format from:

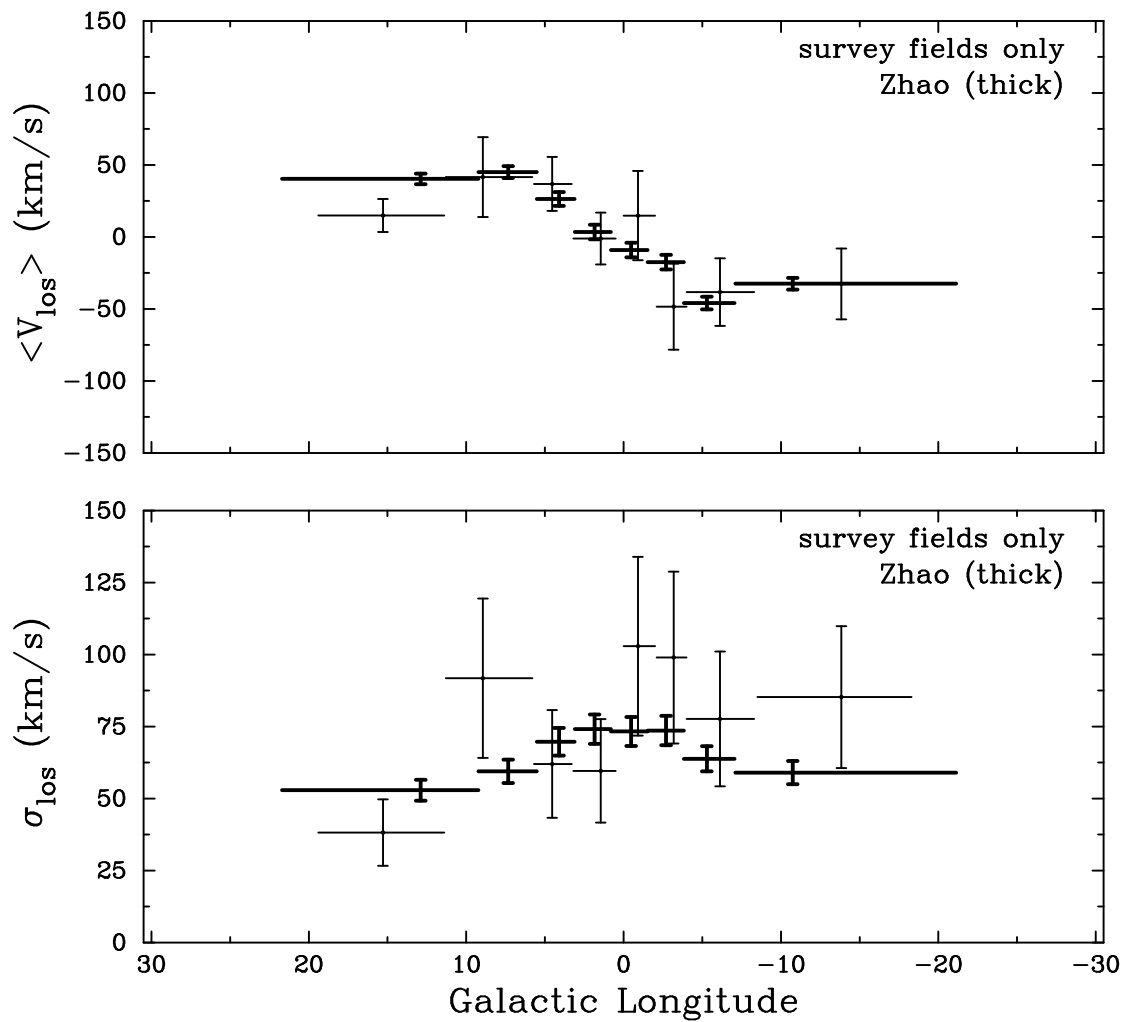
<http://arxiv.org/ps/astro-ph/0005086v1>

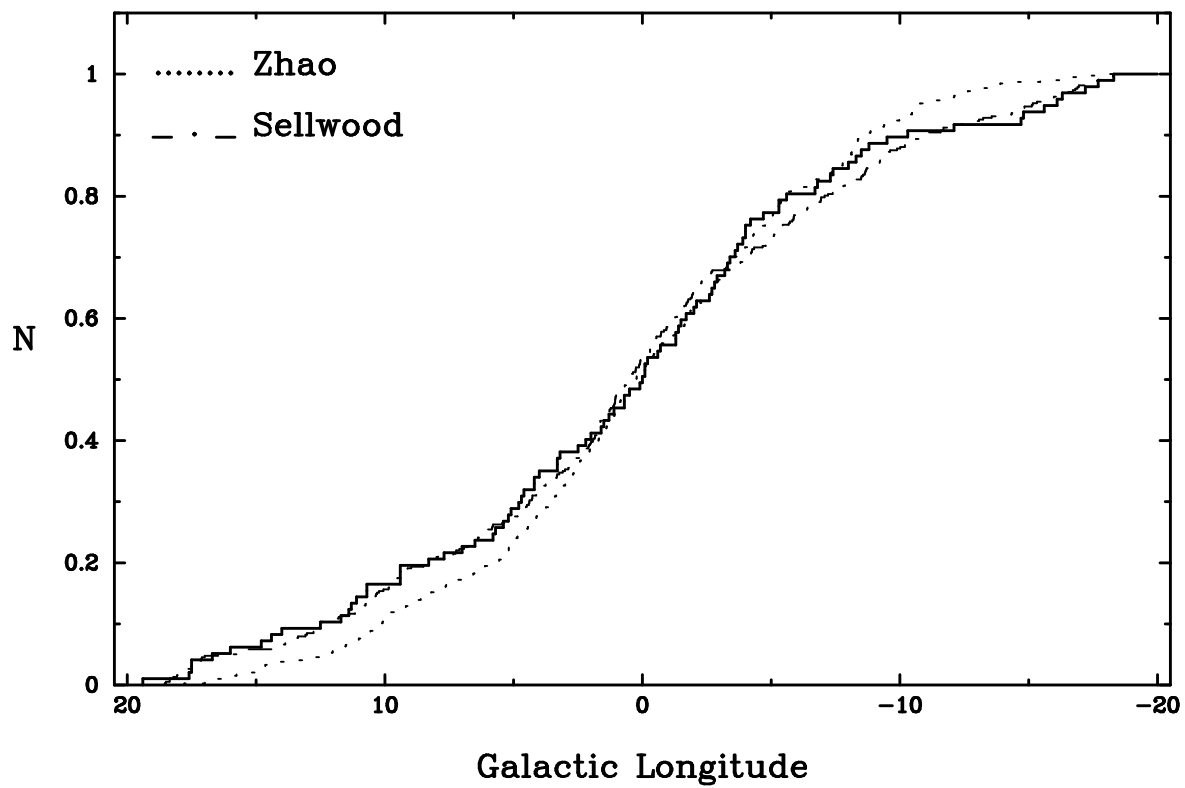
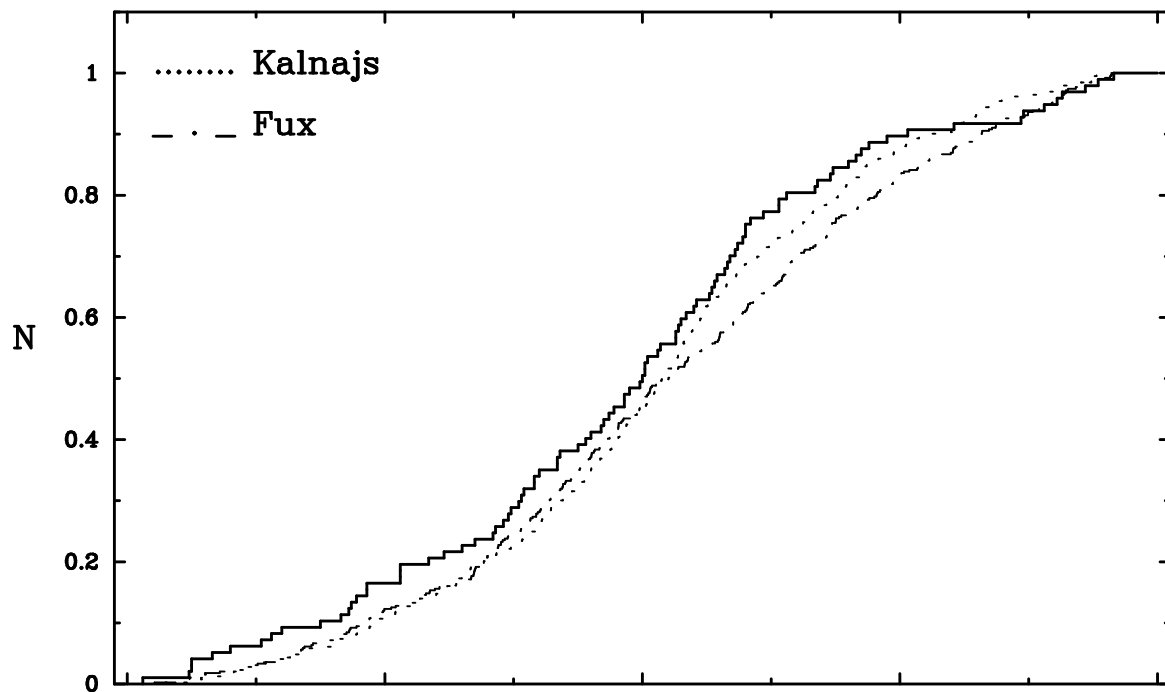












$5 < l < 10$

